J. Fluid Mech. (1987), *vol.* 185, *pp.* 31–65
Printed in Great Britain

Simulation of flow between concentric rotating spheres. Part 2. Transitions

By PHILIP S. MARCUS
Department of Mechanical Engineering, University of California, Berkeley, CA 94720, USA

AND LAURETTE S. TUCKERMAN
Department of Physics, University of Texas, Austin, TX 78712, USA

(Received 22 March 1985 and in revised form 16 March 1987)

We examine the transitions among the steady-state axisymmetric spherical Couette flows with zero, one, and two vortices per hemisphere. The steady flows are reflection symmetric with respect to the equator, but some of the transitions that we find break this symmetry. This is the first study to reproduce numerically the transitions to the one-vortex flow from the zero- and two-vortex flows. In our study, we use a numerical initial-value code to: (i) compute the bifurcation diagrams of the steady (stable and unstable) states, (ii) solve for the most unstable or least stable linear eigenmode and eigenvalue of a steady state, (iii) calculate the velocity field as a function of time during both the linear and nonlinear stages of the transitions, and (iv) determine the energy transfer mechanism into and out of the antireflection-symmetric components of the flow during the transitions.

Our study provides the explanation of the laboratory observation that some transitions occur only when the inner sphere of the Couette-flow apparatus is accelerated or decelerated quickly, whereas other transitions occur only when the acceleration is slow.

1. Introduction

In this paper we examine the time-dependent transitions among steady-state axisymmetric spherical Couette flows. The steady-state solutions were examined by Marcus & Tuckerman in Part 1 (1987). Spherical Couette flows are the equilibria that result when an incompressible, constant-density fluid is constrained between two concentric spheres in which the outer is held stationary and the inner is rotated at an angular velocity Ω_1. There are two non-dimensional control parameters for spherical Couette flow: the Reynolds number $Re \equiv \Omega_1 R_1^2/\nu$ and the gap width between the inner and outer constraining spheres, $\sigma \equiv (R_2 - R_1)/R_1$, where ν is the kinematic viscosity and R_1 and R_2 are the radii of the inner and outer spheres. At low Reynolds numbers spherical Couette flows are found experimentally to be both axisymmetric and reflection-symmetric about the equator (Khlebutin 1968; Sawatzki & Zierep 1970). Three types of spherical Couette flow that exist at medium-gap geometries (i.e. $0.12 \leqslant \sigma \leqslant 0.24$) are characterized by zero, one, and two Taylor vortices on each side of the equator. Wimmer's laboratory experiments (1976) were the first to show that the flows are not unique functions of σ and Re and that the final equilibrium state of the fluid depends also on the history of the fluid – particularly on the rate of acceleration of the inner sphere $\dot{\Omega}_1$ during the transition to a final state.

In this paper we discuss the transitions among the low Re 0-, 1- and 2-vortex flows for the medium gap $\sigma = 0.18$ and for $Re < 1000$. (At $\sigma = 0.18$ there are other steady-state spherical Couette flows. See Schrauf (1983*a*, *b*) and Part 1 for a discussion of these separate solutions.)

Axisymmetric medium-gap 0-, 1- and 2-vortex flows have been previously simulated numerically by other authors using initial-value codes (Bonnet & Alziary de Roquefort 1976; Astaf'eva, Vvdenskaya & Yavorskaya 1978; Bartels 1982; Dennis & Quartapelle 1984). Although these authors have observed numerically the transition from the 0-vortex to the 2-vortex flow (referred to throughout the remainder of this paper as the $0 \rightarrow 2$ transition) and the $1 \rightarrow 0$ transition, the details of the transitions have never been reported in the literature. Furthermore, despite the fact that Wimmer observed the $0 \rightarrow 1$ transition in his laboratory experiments with medium- and narrow-gap flows, the transition has never been produced numerically. For example, Astaf'eva *et al.* successfully simulated several spherical Couette flows in the narrow-gap regime at $\sigma = 0.11$ by expanding the flow in the θ-direction in a truncated 90-term Legendre series and by finite-differencing in the radial direction with 10 grid points. The terms in the Legendre series were chosen so that flow was reflection-symmetric about the equator. Their numerically calculated values of the critical Reynolds numbers for transitions in which the number of Taylor vortices decrease agree with the corresponding experimenal values measured by Yavorskaya, Belyaev & Monakhov (1977) to within 3%. However, Astaf'eva *et al.* were unable to reproduce the $0 \rightarrow 1$ transition at all. Because their code imposed axisymmetry as well as reflection-symmetry about the equator, they were led to the conclusion that the $0 \rightarrow 1$ transition breaks one or both of these symmetries. Astaf'eva *et al.* were only able to simulate the steady-state 1-vortex spherical Couette flow by starting their initial-value code with a 0-vortex flow and artificially adding a large perturbation with one Taylor vortex on either side of the equator. Bartels simulated spherical Couette flows for a range of medium-gap sizes by using a high-resolution finite-difference code. He also noted that he was unable to produce the $0 \rightarrow 1$ transition. His initial-value code computed the flow in the domain $0 \leqslant \theta \leqslant \frac{1}{2}\pi$, and he imposed reflection symmetry about the equator. With $\sigma = 0.17647$, he could only simulate the steady-state 1-vortex flow by modifying his code so that a 'reflection symmetry' was artificially imposed about the $\theta = (\frac{1}{2}\pi + 0.0122)$ plane. Once he simulated the 1-vortex flow he was able to produce the $1 \rightarrow 0$ transition in accord with the laboratory experiments of Wimmer. Speculating that the $0 \rightarrow 1$ transition was caused by velocity perturbations that were asymmetric with respect to the equator, Bartels conducted simulations in the whole $0 \leqslant \theta \leqslant \pi$ domain and allowed round-off errors to produce asymmetric velocity perturbations. However, he was still unable to produce the $0 \rightarrow 1$ transition.

In this paper we produce the $0 \rightarrow 1$ transition that was found experimentally by Wimmer by using an axisymmetric pseudospectral code in which the velocity is computed in the entire $0 \leqslant \theta \leqslant \pi$ domain. We describe this transition as well as the $1 \rightarrow 0$, $0 \rightarrow 2$, and $2 \rightarrow 1$ transitions in §3 of this paper. The $2 \rightarrow 1$ transition at low Reynolds number (i.e. for $Re < 1300$, not to be confused with the $2 \rightarrow 1$ transition at $Re = 3950$ observed by Wimmer 1976) not only has never been simulated prior to this paper but also until very recently had never been observed in the laboratory (K. Bühler, private communication 1983). Our calculations of the transitions are carried out by solving the Navier–Stokes equation as an initial-value problem. The details of the numerical procedure are given in Part 1.

In §2 we present a global view of the transitions by examining the torque–Re

curves of the steady-state equilibria (i.e. the bifurcation diagrams). These curves are very useful for showing which flows are members of the same family of equilibria and which are totally disjoint. Bifurcation diagrams illustrate succinctly the upper and lower bounds in Reynolds number where an equilibrium solution exists and where transitions, both linear and finite-amplitude, are permitted. Schrauf (1983*a*, *b* and private communication) used a numerical steady-state solver to compute bifurcation diagrams for spherical Couette flows with $\sigma = 0.17647$ over a much wider range of Reynolds number than we present in this paper, and he has determined many independent families of solutions. The advantage of a steady-state solver over an initial-value code is that the former converges to an equilibrium solution even when it is unstable. Our initial solver cannot usually converge to unstable solutions. (In general, we can only converge to an unstable equilibrium if the unstable modes of the equilibrium can be suppressed by artificially imposing a spatial symmetry.) A disadvantage of a steady-state solver is that as the user increases the spatial resolution, the computational cost usually increases much faster than it does with an initial-value code. In the Reynolds-number regime where our results and Schrauf's overlap, there is good agreement between the bifurcation diagrams with one important exception that is discussed in §2.

In §3 we compute the time-dependent transitions using our initial-value solver, and illustrate the evolution of the flow during transition by plotting temporal sequences of the meridional streamlines and profiles of the azimuthal component of the velocity. We also plot the torques on the inner and outer spheres.

Many authors have previously examined transitions in spherical Couette flows by first numerically calculating a 0-vortex equilibrium and then determining its linear eigenmodes (Bratukhin 1961; Yakushin 1969; Munson & Menguturk 1975; Walton 1978; Soward & Jones 1983). These calculations were restricted to narrow- and wide-gap geometries. The calculations determined critical Reynolds numbers for linear instability of 0-vortex flow to a secondary flow. Munson & Joseph (1971) used an energy method that allowed them to examine finite-amplitude instabilities as well. Examining wide-gap flows with $\sigma = 1$, Munson & Menguturk found that the eigenmode of the linear instability associated with the critical *Re* was axisymmetric and antisymmetric with respect to the equator. In contrast to that linear analyses, Munson & Joseph's energy analyses of the same flow showed that the instability was not only asymmetric with respect to the equator but also not axisymmetric. Examining narrow-gap flows, Yakushin determined the critical *Re* for the onset of Taylor vortices at $\sigma = 0.1$, and Walton and Soward & Jones determined the value in the limit $\sigma \to 0$. Their results agree with the experimentally measured values to within 3%. The linear instabilities that they found correspond to transitions from the 0-vortex flow to flows with many (i.e. more than 30) Taylor vortices. Not surprisingly, the critical Reynolds numbers for the onset of Taylor vortices in spherical Couette flows with narrow gaps is close to the value for the onset of Taylor vortex flow in cylindrical geometries.

In §4 we present our calculations of the linear eigenmodes that produce the $0 \to 1$ and $2 \to 1$ transition. Using the results of our linear stability calculations we show why it is easy to miss these transitions in both the numerical simulations and also in the laboratory measurements. In §5 we plot the time-development of the energy and examine how the kinetic energy is transferred among the different modes during transitions; this transfer is particularly helpful in understanding the role of symmetry and nonlinearity in the transitions. Our conclusions appear in §6.

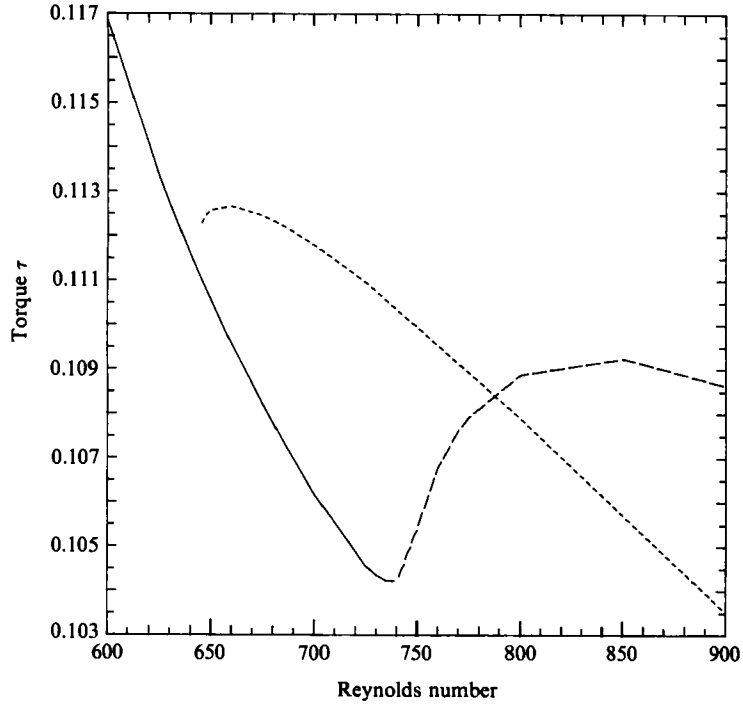

FIGURE 1. Bifurcation diagram showing the torques of the ——, 0-vortex, – – –, 1-vortex, and — — —, 2-vortex flows as a function of Re with $\sigma = 0.18$. The meeting of the 1-vortex and 0- and 2-vortex curves at $Re \approx 790$ is a projection effect and not a bifurcation. The 0- and 2-vortex equilibria are linearly unstable for $651 < Re < 775$.

2. Bifurcation diagram

2.1. *The* 0- *and* 2-*vortex equilibrium and the* 1-*vortex equilibrium curves*

Figure 1 shows the torque τ as a function of Re for our numerically computed steady-state equilibrium flows at $\sigma = 0.18$. (We have non-dimensionalized the torque and all other quantities throughout this paper unless stated otherwise, with R_1 as the unit of length, Ω_1^{-1} as time, and ρR_1^3 as mass, where ρ is the fluid density. The torques of the 0-vortex (solid curve), the 1-vortex (short-dashed curve), and the 2-vortex (long-dashed curve) flows were computed in increments of 10 in the Reynolds number except in regions of rapid change (see below) where the increments were finer. (The curves in figure 1 are drawn as straight line segments between our numerically computed data points.)

A striking feature of the bifurcation diagram, discovered independently by Schrauf (1983*b*) and by ourselves, is that the 0-vortex and 2-vortex flows lie on the same curve and are therefore part of the same equilibrium family. The 0-vortex flow evolves smoothly into the 2-vortex flow (with the critical Re for the onset of 2-vortex flow defined to be the Re at which pinched streamlines close to form recirculation vortices – see §3). We have found that the critical Re is $740 \pm (0.05)$. As we showed in Part 1, one of two pairs of Taylor vortices in 2-vortex flow (the pair farther from the equator) has zero diameter at the critical Re. As Re increases, the small vortex pair rapidly grows in size (and intensity) and increases the torque. Because of the

large change in τ near the critical Re, we have computed equilibria for seven values of Re in the range $730 \leqslant Re \leqslant 745$.

Schrauf (1983*a*, *b*) discovered that the 1-vortex flows lie on a curve distinct from that of the 0- and 2-vortex flows, and the two curves never intersect. The fact that figure 1 shows that two curves cross near $Re = 785$ is a two-dimensional projection effect due to the fact that we have represented each flow by only one parameter, the torque. If we had plotted the torques and the vortex size (for example) for each of the flows as a function of Re, we would find that the two equilibrium curves (which would now be imbedded in a three-dimensional space) never intersect.

The 0- and 2-vortex equilibrium curve extends beyond the left- and right-hand boundaries of figure 1. It extends to the left to $Re = 0$ where it becomes the Stokes solution. The 1-vortex curve extends to the right beyond the border of figure 2 but not to the left. At $Re = 645 \pm 0.05$ we find that the 1-vortex curve has a turning point (or one-sided bifurcation) where the slope becomes infinite. To calculate Re at the turning point, we computed four equilibria in the interval $645 \leqslant Re \leqslant 650$. (The turning point is also shown dramatically in figure 3 of Part 1 where we plotted the sizes of the vortex in the 1-vortex flow as a function of Re). At $Re \approx 645$ the 1-vortex equilibrium curve cannot end abruptly but must turn around and continue back towards the right-hand side of the figure. At the present time we are unable to compute this half of the curve with our initial-value code, since it represents an unstable equilibrium, but Schrauf (1983*b*), working with a steady-state solving code and a gap width close to 0.18 ($\sigma = 0.17647$) not only computed the unstable half of the 1-vortex curve but also found that it never intersects the 0- and 2-vortex curve. Although they have not been observed by experimentalists, Schrauf calculated additional equilibria that exist for $Re \gtrsim 800$ and consist of stable 0- and 2-vortex states.

Convergence of our initial-value code does not necessarily imply the linear stability of the solution. (For example, our code can converge to an equilibrium that is unstable to anti-reflection-symmetric modes if these modes are excluded from the computational domain.) In fact, we show in §4 that the portion of the 0- and 2-vortex equilibrium curve for $651 < Re < 775$ is linearly unstable.

2.2. *Turning points and other bifurcations*

Figure 1 shows that the stable equilibria are non-unique for $645 \leqslant Re \leqslant 651$ and $775 \leqslant Re \leqslant 900$. Non-uniqueness of solutions is a well-established property of the Navier–Stokes equation, but it is also well known that for low values of Re the flow is unique (Serrin 1959). Uniqueness at $Re = 0$ implies that except for the one equilibrium curve that becomes the Stokes solution all other equilibrium curves must have (one or more) one-sided bifurcations, where the slopes become infinite and the curves turn around. The turning point of the 1-vortex curve at $Re = 645$ can be thought of as a consequence of the uniqueness of the Navier–Stokes equation at low Re.

The feature of figure 1 that may seem somewhat surprising is that there are no true intersections of the equilibrium curves. The equilibria of many classical flows, such as Rayleigh–Bénard convection or Taylor–Couette flow in infinitely long cylinders, do intersect, and due to the symmetry of the flows the intersections result in symmetric bifurcations in the sense that the point of intersection is coincident with the turning point of one of the equilibrium curves (i.e. pitchfork bifurcations). Consider, for example the transition from circular Couette flow (between infinitely long cylinders)

to axially periodic Taylor vortex flow (Kirchgassner & Sorger 1968; Kogelman & Di Prima 1970). Each wavelength of such a flow contains two Taylor vortices of opposite circulation. Two Taylor vortex states can be chosen by setting the phases such that the inflow or outflow boundaries of the vortices coincide with the boundaries of the periodic domain. These flows are physically equivalent. The bifurcation associated with the onset of Taylor vortices is therefore a pitchfork bifurcation. (Actually, if we could draw a three-dimensional bifurcation curve we would show the pitchfork as a paraboloid of revolution with the angle around the paraboloid equal to the axial phase of the Taylor vortices.)

Suppose now that we impose finite axial-length boundary conditions but make the unphysical assumption that the axial endplates rotate differentially with the same velocity as circular Couette flow (so that circular Couette flow is still an exact solution). This serves the purpose of breaking the equivalence between states with an even number of Taylor vortices, since states with inflow near the axial boundaries are now physically distinct from those with outflow near the boundaries. Transitions to such states are now associated with transcritical rather than pitchfork bifurcations. Finite axial-length boundaries also introduce a second class of solutions. These are the antisymmetric states or those with an odd number of vortices. Antisymmetric states with outflow near the top axial boundary and with inflow near the bottom are equivalent to states with inflow near the top and outflow near the bottom. This equivalence is associated with a symmetric pitchfork bifurcation. Considerations of symmetry have been extensively discussed by Benjamin (1978*a*, *b*), and we shall return to them presently.

2.3. *Decoupling of bifurcation diagrams*

Bifurcations can do more than change character: they can disappear altogether. For example, figure 2(*a*) shows schematically a transcritical bifurcation between two curves. One curve (the straight horizontal line) is stable (indicated by the solid curve) for $0 \leqslant Re \leqslant Re_{\mathrm{b}}$ and unstable (indicated by a dotted line) for $Re_{\mathrm{b}} \leqslant Re < \infty$. The second curve drawn as a horizontal parabola has a turning point at Re_{t}; it contains one unstable and two stable portions. The bifurcation for the transition from the circular Couette flow discussed above (with the finite axial-length but artificial boundary conditions) to a Taylor-vortex flow with an even number of vortices looks like figure 2(*a*). The straight horizontal line represents qualitatively the primary circular Couette flow, and the parabolic curve with the turning point represents the secondary Taylor-vortex flow. When the endplates are stationary or rotate with uniform angular velocity as in real experiments, Ekman pumping produces a meridional flow. This causes the bifurcation to be decoupled (Benjamin 1978*a*, *b*), as in figure 2(*b*). Intuitively, we expect spherical Couette flow to be more similar to Taylor–Couette flow with stationary or uniformly rotating endplates. Our bifurcation diagram of spherical Couette flow in figure 1 looks qualitatively like figure 2(*b*), with the solid lower curve of the latter figure representing the 0- and 2-vortex flow branch and the solid or stable half of the upper curve with the turning point representing the stable part of the 1-vortex flow (which has an even number of Taylor vortices).

Benjamin & Mullin's (1982) study of finite-length cylindrical Couette flow showed that the transition from a primary circular-Couette-like (i.e. 0-vortex) flow takes place continuously as a function of *Re*. They found that for large *Re*, axisymmetric Taylor-vortex flows are non-unique, and that flows with the 'preferred number' of vortices lie on the same equilibrium curve as the primary 0-vortex circular-Couette-like flow. Equilibrium flows with different numbers of Taylor vortices lie on distinct

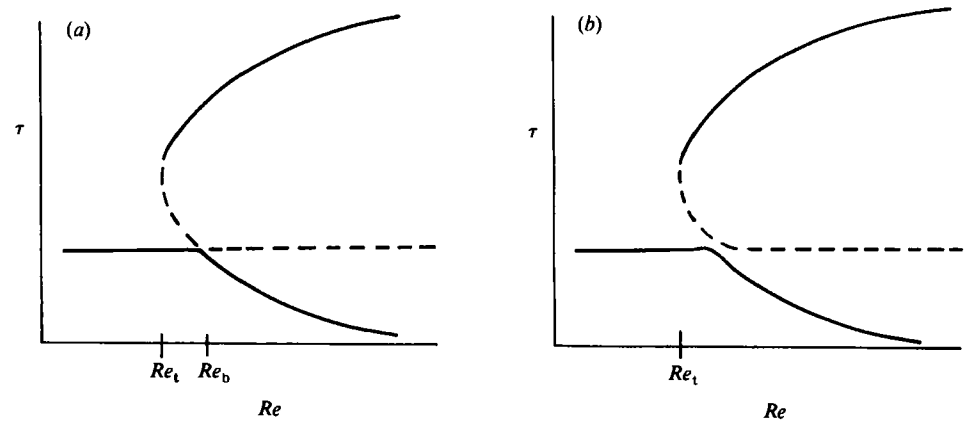

FIGURE 2. (*a*) Schematic diagram showing a transcritical bifurcation. There are two equilibrium curves, one represented by a horizontal straight line and the other by a parabola lying on its side. At the turning point of the parabola Re_t and at the bifurcation point Re_b (where the two stable curves intersect) the solutions change from being stable (solid curve) to unstable (dotted curve). (*b*) Decoupling of the bifurcation diagram of (*a*) showing no intersection. Solutions lying on the straight horizontal line at low and high Re are no longer part of the same equilibrium family. Re_t still exists but Re_b does not.

curves that do not intersect the curve of the primary flow. Benjamin & Mullin's finding is analogous to what we find in spherical Couette flow for $\sigma = 0.18$: the 2-vortex flow is the 'preferred' flow that is part of the primary 0-vortex equilibrium curve, and the 1-vortex flow equilibrium (with a non-preferred number of vortices) lies along a distinct, non-intersecting curve.

Another possible way in which perturbations can change a bifurcation is shown schematically in figure 3. In figure 3(*a*) there are two distinct curves; one stable, the other unstable. Neither curve has a turning point, and a stable solution exists for all Re. We have found that numerically induced perturbations can change figure 3(*a*) into figure 3(*b*). The two curves in figure 3(*b*) have turning points Re_{t1} and Re_{t2}. No solution (stable or unstable) exists for $Re_{t1} < Re < R_{t2}$. In particular we have found that the 1-vortex flow at $\sigma = 0.18$ lies on a stable, continuous equilibrium curve like the lower solid curve in figure 3(*a*) for $1300 \geqslant Re \geqslant 645$. (We have not explored $Re > 1300$.) Using finite-differences with 11 radial and 121 azimuthal grid points per hemisphere, Schrauf (1983*b* and private communication) found that the 1-vortex flow equilibrium with $\sigma = 0.17647$ and with Re near 1200 lies along a curve that looks qualitatively like figure 3(*b*). He found two turning points with $Re_{t1} = 1065$ and $Re_{t2} = 1300$ and concluded that there was a range of Reynolds numbers between the two turning points for which there was no 1-vortex flow solution.

To resolve this inconsistency, we computed stable 1-vortex flows at $Re = 1200$ (i.e. between Schrauf's two turning points where the equilibrium should not exist) using 32 radial and 256 azimuthal collocation points and again with 16 radial and 128 azimuthal points. Both of our computed flows were stable and nearly identical to each other. When the numerical resolution was then reduced to 8 radial and 64 azimuthal collocation points the flow changed from the 1-vortex flow to the 2-vortex flow indicating that the stable 1-vortex equilibrium ceased to exist. The results of this numerical experiment are consistent with the bifurcation diagram changing from figure 3(*a*) to figure 3(*b*) due to numerical spatial resolution errors.

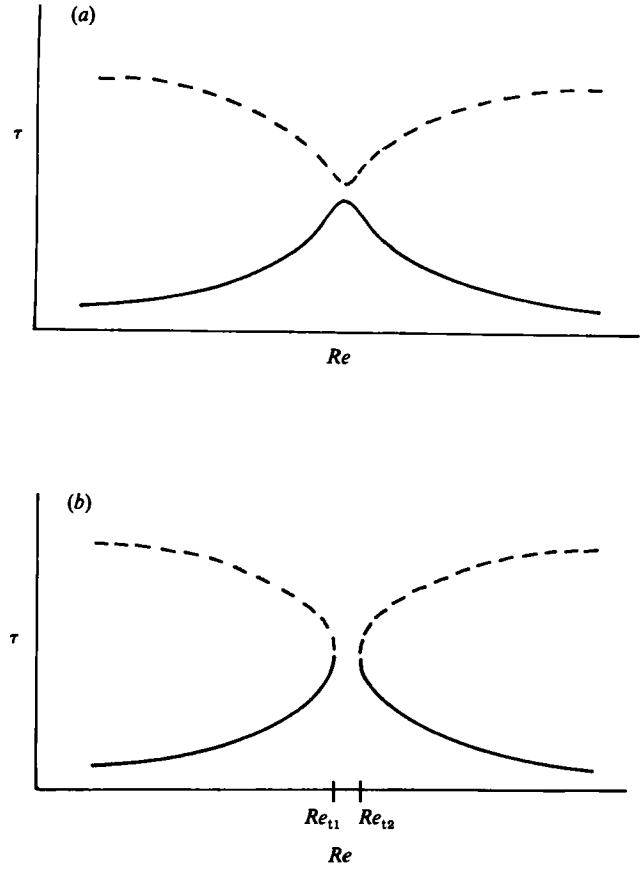

FIGURE 3. (*a*) Schematic diagram showing two equilibrium curves, ——, stable and – – –, unstable. Both curves exist for all Re. (*b*) Decoupling and merging of the two equilibrium curves of figure 3(*a*). At the turning points Re_{t1} and Re_{t2} the stability of the equilibria change. For $Re_{t1} < Re < Re_{t2}$ there are no equilibrium solutions.

2.4. *Bifurcation in the presence of symmetry*

A necessary condition for an equilibrium curve to change from stable to unstable (or vice versa) is the presence of a turning point or an intersection. Since the 0- and 2-vortex equilibrium curve changes from stable to unstable at $Re = 651$ and regains stability at $Re = 775$ (as we shall discuss in §4), and since there are clearly no turning points, there must be bifurcation points caused by intersection with other equilibrium curves.

If the bifurcation at $Re = 651$ were transcritical or supercritical (or at $Re = 775$ transcritical or subcritical) there would be additional stable equilibrium branches intersecting the 0- and 2-vortex equilibrium curve. Experiments and initial-value calculations should be able to find these branches at Re just greater than 651 (and Re just less than 775); the absence of such stable equilibria (as we shall discuss in §3) leads to the conclusion that the bifurcation at $Re = 651$ is a subcritical pitchfork and that at $Re = 775$ a supercritical pitchfork.

There is another reason for the necessity of symmetric pitchfork bifurcations at $Re = 651$ and 775 which is related to our earlier discussion of the role of symmetry. The geometry of spherical Couette flow is, of course, equatorially symmetric. Any

asymmetric state can be written as the sum of a reflection-symmetric piece $\boldsymbol{u}_R$ and an antireflection-symmetric piece $\boldsymbol{u}_A$. If $(\boldsymbol{u}_R+\boldsymbol{u}_A)$ is an equilibrium, then equatorial symmetry implies that $(\boldsymbol{u}_R-\boldsymbol{u}_A)$ is also an equilibrium. This is the condition necessary for the existence of a pitchfork bifurcation.

We show in §4 that the eigenmodes to which the 0- and 2-vortex flows are unstable at $Re = 651$ and $Re = 775$ are antireflection-symmetric. The corresponding unstable equilibria that intersect the 0- and 2-vortex as subcritical and supercritical pitchfork bifurcations respectively must therefore be asymmetric with respect to the equator. These asymmetric equilibria could not, of course, be detected by Schrauf (1983*b*) with this equatorially reflection-symmetric steady-state finding code. When made aware of the existence of the antireflection-symmetric eigenmodes (Tuckerman 1983), Schrauf & Krause (1984) subsequently found the subcritical bifurcation near $Re = 651$ by generalizing their code to allow for asymmetric equilibria.

2.5. *Transitions allowed by the bifurcation diagram*

Without understanding any of the details of the physics of the spherical Couette flows we can still determine where transitions between flows are allowed and expected by using the bifurcation diagram in figure 1 (disregarding the possible presence of stable equilibrium curves other than the two shown in the figure for $Re < 900$). For example, for $Re < 645$ all initial conditions no matter how contrived lead to the 0-vortex flow because 0-vortex flow is the unique stable solution for $Re < 645$. This means that if a 1-vortex flow is created at $Re = 645$ and if Re is then lowered to 644 a $1 \rightarrow 0$ transition must occur. For $645 \leqslant Re \leqslant 651$ an initial condition can lead to either the 0- or the 1-vortex flow. Each of the two linearly stable equilibria has its own basin of attraction, and all initial conditions belong to one of the two attracting basins. The flows are stable to finite-amplitude disturbances if and only if the nonlinear disturbance keeps the flows inside their original basins of attraction. However, the relative size of the two basins can be determined only by performing large numbers of initial-value experiments.

For $651 < Re < 775$, the 0- and 2-vortex equilibria are linearly unstable, as we show in §4, but the growth rate of the linear instability is slow. By varying Re rapidly compared to the instability's growth rate, the flow can therefore be made to march along the entire length of the 0- and 2-vortex equilibrium curve in figure 1. Another way of creating the $0 \rightarrow 2$ transition is to start with a stable 0-vortex flow (i.e. $Re \leqslant 651$) and then suddenly change Re to Re_2, with $Re_2 \geqslant 775$ (where the 2-vortex flow is stable), provided that the flow does not stumble into the basin of attraction of the 1-vortex equilibrium flow at Re_2. However, this transition will not proceed along the path of the 0- and 2-vortex equilibrium curve in figure 1 (see §3).

If the 0- or 2-vortex equilibria are created with $651 < Re < 775$ and if we wait long enough a transition to a 1-vortex state should be observed. In particular, if a 0-vortex flow is created at 651 and Re is changed to 652 a $0 \rightarrow 1$ transition occurs. If a 2-vortex flow is created at 775 and Re is then reduced to 774, a $2 \rightarrow 1$ transition occurs. For $Re \geqslant 775$ the 2-vortex and 1-vortex flows are both stable to linear perturbations, and each has its own basin of attraction which determines its stability with respect to nonlinear perturbations. The 1-vortex flow for $Re < 900$ is always linearly stable, and for $651 < Re < 775$ it is stable to nonlinear perturbations as well. We therefore do not expect to see a $1 \rightarrow 2$ transition, except for $Re > 775$ and then if and only if a finite amplitude perturbation is introduced that is sufficiently large to take the 1-vortex flow out of its attracting basin.

We note that the $1 \rightarrow 0$ and $0 \rightarrow 1$ transitions that are caused by infinitesimal

changes in Re occur respectively at $Re = 645$ and $Re = 651$. This type of hysteresis is a common feature of hydrodynamic flows whose transitions are not due to supercritical bifurcations.

3. Physical description of the transitions

3.1. $0 \rightarrow 2$ *transition*

We have shown in §2 that the $0 \rightarrow 2$ transition can be produced by starting with a stable 0-vortex equilibrium ($Re \leqslant 651$) and then suddenly increasing Re to a value greater then 775 where the 2-vortex equilibrium is stable. We illustrate this transition here by starting with a flow at $Re = 0$ (the Stokes flow) and suddenly increasing Re to 800. In figures 4 and 5 we show a time-sequence of projections of the velocity that illustrate the temporal evolution of the flow during the $0 \rightarrow 2$ transition. Although the flows that we show are not equilibria, the evolution of the flow with increasing time qualitatively resembles the succession of steady states along the 0- and 2-vortex curve with increasing Reynolds number.

At time $t = 0$ we begin our transition with the 0-vortex Stokes flow at $Re = 0$. The flow is purely azimuthal, and there is no meridional or (r, θ)-component of the flow (see Part 1, equation (2.5)). Re is raised instantaneously to 800 (by lowering the viscosity of the fluid), and the flow begins to evolve quickly. Figure 4 shows the meridional component of the velocity (which is always reflection-symmetric about the equator) at times $t = 2\pi$, 4π, 6π, 8π, 10π, and 40π. (In our dimensionless units the period of the inner rotating sphere is 2π; the viscous diffusion time from the inner to outer sphere is $Re\,\sigma^2 = 25.92$ and the diffusion time from pole to equator is $\frac{1}{4}\pi^2 Re = 1974$). The quantities that we have plotted in figure 4 are the contours of constant stream function $\psi r \sin\theta$, where the meridional component of the velocity is derived from ψ by

$$u_r = \frac{1}{r \sin\theta} \frac{\partial}{\partial \theta} (\psi \sin\theta), \tag{3.1}$$

$$u_\theta = -\frac{1}{r} \frac{\partial}{\partial r} (r\psi). \tag{3.2}$$

The meridional component of the velocity is therefore tangent to the contours of constant $[\psi r \sin\theta]$.

The velocity that we have graphed in the figure is the solution of the Navier–Stokes equations that we compute numerically by the methods of Part 1. Solid contours represent counterclockwise, and short-dashed contours clockwise meridional flow. There is an outflow boundary at the equator in all of the flows in figure 4. We have only shown the flow in the domain near the equator $\frac{3}{8}\pi \leqslant \theta \leqslant \frac{5}{8}\pi$. The flow in the domain $0 \leqslant \theta < \frac{3}{8}\pi$ and $\frac{5}{8}\pi < \theta < \pi$ does not change qualitatively during the $0 \rightarrow 2$ transition and is just the continuation of the two (large basic) vortices of figure 4(*a*). (See figures 4, 7, 10, and 13 in Part 1 for examples of the meridional flow in the entire $0 \leqslant \theta \leqslant \pi$ domain.) The tick marks along the outer radius in figure 4 are equally spaced with the circumferential difference between ticks equal to σ.

Figure 4(*a*) shows that by time $t = 2\pi$ the flow has a large basic vortex (unrelated to a Taylor vortex, see Part 1, §4) extending from the equator to the pole in each hemisphere. The flow looks qualitatively like the steady-state equilibrium flow at $Re = 600$ (see figure 4, Part 1). After two rotations of the inner sphere, the flow develops a pinch or stagnation point in each hemisphere as shown in figure 4(*b*) at

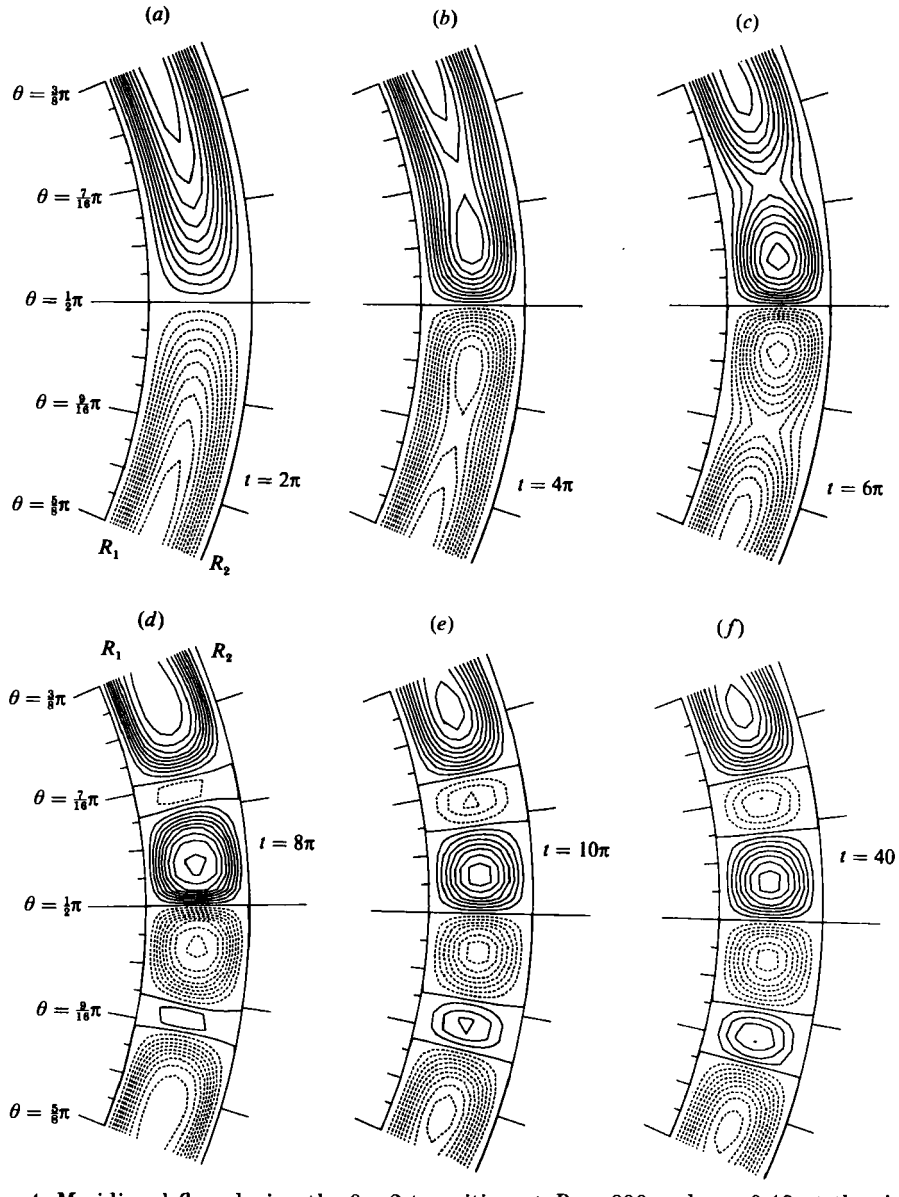

FIGURE 4. Meridional flow during the $0 \rightarrow 2$ transition at $Re = 800$ and $\sigma = 0.18$ at the six times indicated on the figure. Streamlines with counterclockwise circulation are shown by solid curves and those with clockwise circulation by dashed curves. The tick marks on the outer radius have circumferential spacings equal to the gap width.

$\theta = \frac{7}{16}\pi$ and $\frac{9}{16}\pi$. By $t = 6\pi$ the pinches have developed further and we see clearly that $\psi r \sin\theta$ has two local maxima or minima in each hemisphere. Figure 4(*c*) shows a flow that looks similar to the steady-state equilibrium 0-vortex flow with pinches at $Re = 650$ (figure 7, Part 1).

At a time between 6π and 8π the pinch in each hemisphere near the equator breaks off and forms a nearly straight radial streamline at $\theta \approx \frac{7}{16}\pi$ (in fact, a zero-diameter Taylor vortex) that goes all the way from the inner to the outer sphere. This event is the delimiter between a 0-vortex flow with pinches and a 2-vortex flow.

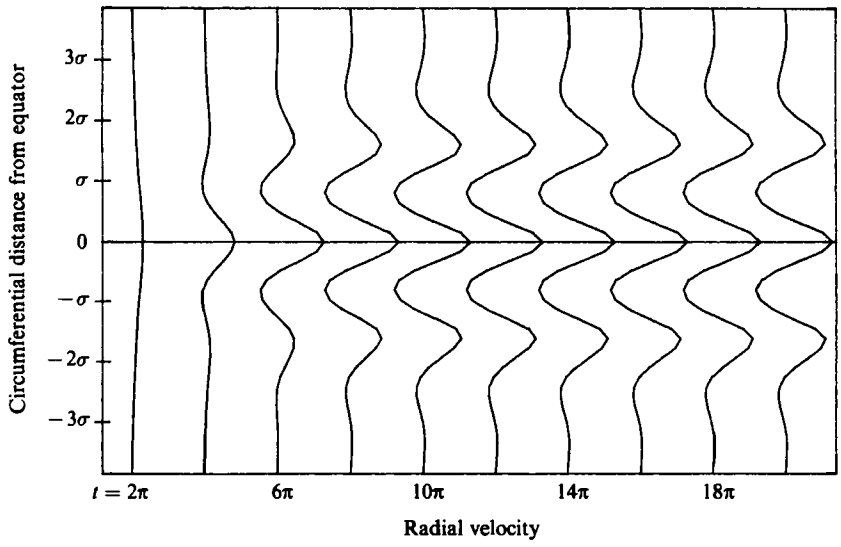

FIGURE 5. Radial velocity $u_r(r = \bar{r}, \theta, t)$ profiles during the $0 \rightarrow 2$ transition where $\bar{r} \equiv \frac{1}{2}(1+\sigma)$. The profiles are labelled along the abscissa by the times at which they occur. The velocity profiles all have the same horizontal scale; deviations to the right (left) indicate radially outward (inward) flow. The maximum radial velocity shown is 0.088 in dimensionless units.

The diameter of this vortex increases monotonically with time and figure 4(*d*) shows that it grows to become a recirculation Taylor vortex, i.e. it has a circulation opposite to that of the large basic vortex and the newly formed larger Taylor vortex. The Taylor vortices are separated from each other at the equator and from the large basic vortex by nearly straight radial streamlines that begin and end at the inner and outer spheres. By $t = 10\pi$ the formation of the 2-vortex flow is nearly complete. This time corresponds to five inner sphere rotation periods or 1.212 diffusion times from the inner to outer sphere. Between $t = 8\pi$ and 10π the recirculation Taylor vortex grows in size and strength in a manner that is analogous to its growth with increasing *Re* in the steady-state equilibria. A completely steady state is reached by $t = 40\pi$. Note that the entire $0 \rightarrow 2$ transition shown in figure 4 is reflection-symmetric about the equator.

Figure 5 shows the radial velocity $u_r(r = \bar{r}, \theta, t)$ as a function of θ and t for the $0 \rightarrow 2$ transition of figure 4 where $\bar{r} \equiv \frac{1}{2}(1+\sigma)$. Each velocity profile is labelled along the abscissa by the time at which it occurs and along the ordinate by the distance from the equator in units of gap size (only the equatorial region is shown). Within each profile, the distance along the abscissa also measures the magnitude of $u_r(r = \bar{r}, \theta, t)$. All the profiles are plotted with the same velocity scale, so figure 5 provides a quantitative comparison of the magnitude of the meridional flow at different times and locations. The maximum velocity in the figure is 0.088 in our dimensionless units. Deviations of the velocity profile to the right (left) indicates radially outward (inward) flow; so, for example, the figure shows clearly that there is always an outward radial flow at the equator. The radial velocity profiles in figure 5 cannot distinguish between the Taylor vortices of the 2-vortex flow and the pinches of the 0-vortex flow. For example, at a distance of 1.7σ from the equator, the velocity is radially outward along the boundary between the large basic vortex and either the recirculating Taylor vortex in the case of the 2-vortex flow, or the velocity on the poleward side of the stagnation point in the case of the 0-vortex flow. These cannot

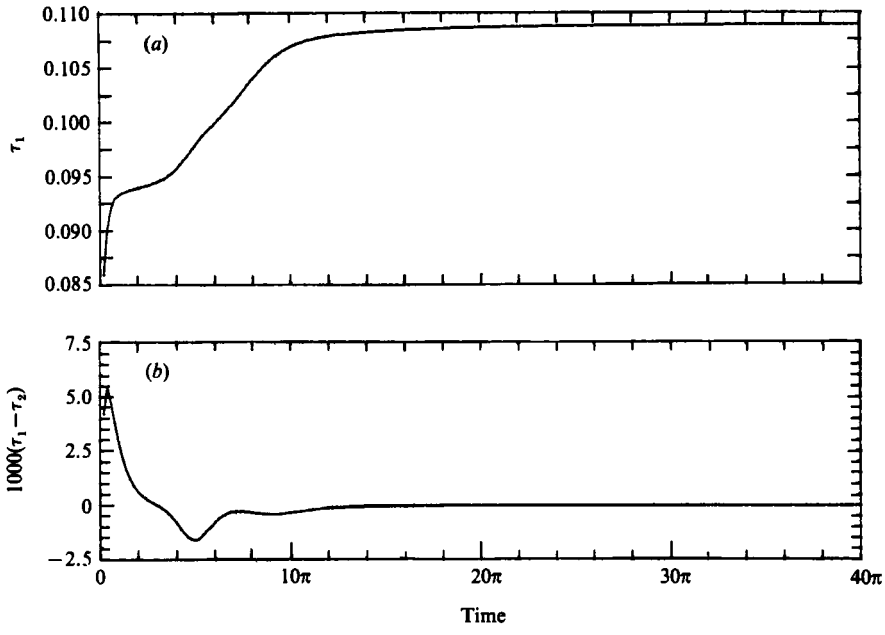

FIGURE 6. (*a*) Torque at the inner sphere τ_1 as a function of time during the $0 \rightarrow 2$ transition. (*b*) Difference between the torques at the inner and outer spheres $(\tau_1 - \tau_2)$ during the $0 \rightarrow 2$ transition. $(\tau_1 - \tau_2)$ is equal to the time derivative of the fluids angular momentum. Note that the vertical scales on (*a*) and (*b*) are different.

be distinguished from each other in figure 5. Note that the characteristic *Re* of the meridional velocity based on the gap size, the maximum value of u_r, and ν is about 12. Recirculation vortices of the type shown in figure 4 generally form in two-dimensional flows at Reynolds numbers of about 12 (cf. Taneda 1979).

The torque at the inner sphere $\tau_1(t)$ and the difference in torque between the inner and outer spheres $[\tau_1(t) - \tau_2(t)]$ as a function of time are shown in figure 6. The difference between the torques is equal to the time rate of change of the flow's angular momentum. Note that figures 6(*a*) and (*b*) do not have the same scale along the ordinate. The very rapid increase in τ_1 for $0 \leqslant t < \pi$ is due to the instantaneous change in *Re*. Interestingly, the plateau-like interval at $\pi \leqslant t \leqslant 4\pi$ is also seen in Wimmer's experiments (private communication, 1983). For $t > 4\pi$ the torque τ_1 increases rapidly with time as the pinches (and later, for $t \geqslant 8\pi$, as the Taylor vortices) increase the radial flux of angular momentum outward from the inner sphere. Initially for $t < 3\pi$, τ_1 is greater than τ_2, but later the inequality reverses. This is consistent with a burst of angular momentum flux leaving the inner sphere at $t = 0$ and arriving at the outer sphere at $t = 3\pi$. The length of time is approximately equal to the gap width divided by the characteristic radial velocity at early times.

3.2. $1 \rightarrow 0$ *transition*

The meridionial circulation of the $1 \rightarrow 0$ transition at four different times is shown in figure 7. At $t = 0$ the flow is the steady, stable 1-vortex flow at $Re = 645$. The transition is initiated at $t = 0$ by abruptly lowering *Re* to 644 (by increasing the viscosity) where the 1-vortex equilibrium no longer exists (see figure 1). For $t > 0$, the recirculating Taylor vortices near the equator monotonically decrease their diameter and energy. The transition proceeds almost imperceptibly until about $t = 100\pi$.

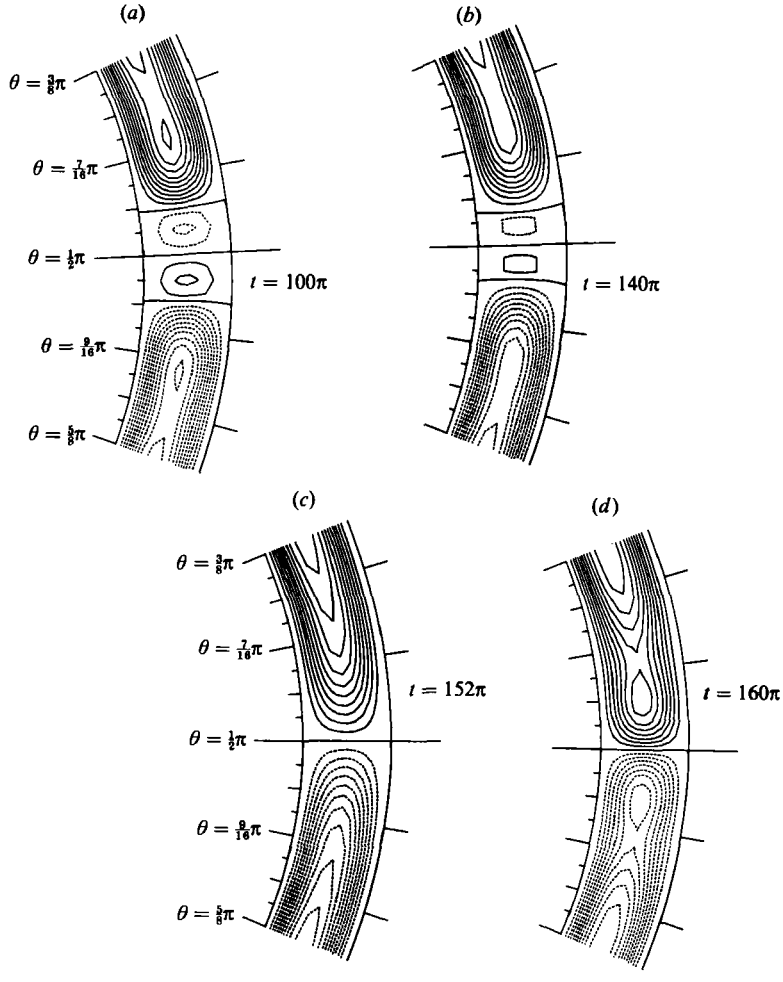

FIGURE 7. Meridional flow plotted as in figure 4 during the $1 \to 0$ transition at $Re = 644$ at the four times indicated.

Figure 7(*a*) shows that the flow at $t = 100\pi$ is similar to the equilibrium flow at $t = 0$ in that each hemisphere has a recirculation vortex near the equator with circumferential size $\approx \frac{2}{3}\sigma$. The large basic vortices in each hemisphere have stagnation points about two gap widths from the equator. At $t = 140\pi$ (figure 7*b*) the recirculating equatorial Taylor-vortex pair has reduced its diameter and has vanished by $t = 152\pi$ (figure 7*c*), leaving a 0-vortex non-equilibrium flow without pinches or stagnation points. By $t = 160\pi$ the flow has nearly reached a steady state, and pinches have reformed in the large basic vortex. The entire $1 \to 0$ transition is reflection-symmetric about the equator. It is slow–on the order of the viscous diffusion time between the equator and pole.

The plots of the radial velocity u_r ($r = \bar{r}, \theta, t$) in figure 8 make especially clear how the equator changes from an inflow to an outflow boundary. At $t = 152\pi$, when the Taylor vortices have just disappeared but the pinches in the large basic vortices have not yet formed, figure 7(*c*) shows that there is a radial outflow boundary at the equator, but figure 8 shows that it is very weak. A strong outflow does not occur at the equator until the pinch has formed. For $t \lesssim 152\pi$ there is a radial outflow at

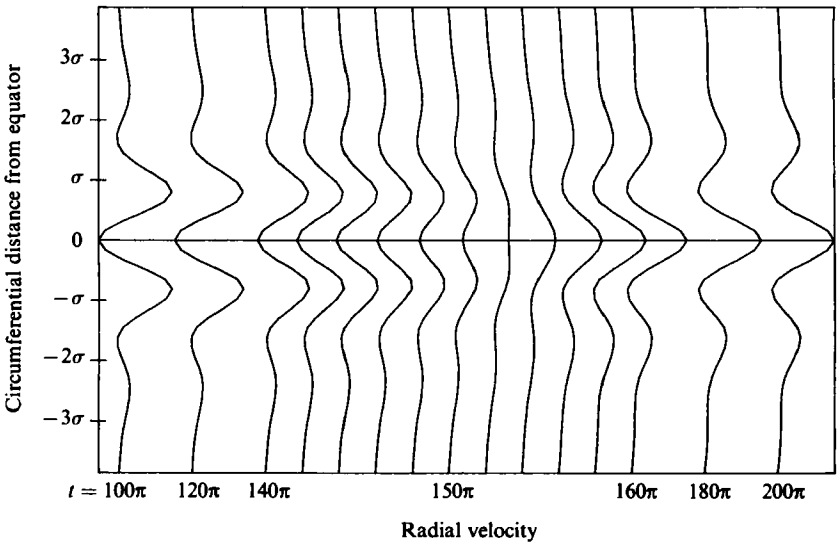

FIGURE 8. Radial velocity, plotted as in figure 5, during the $1 \rightarrow 0$ transition. Note that the inflow radial boundary at the equator becomes an outflow boundary. The maximum radial velocity in the figure is 0.034.

approximately 0.8 gap widths from the equator caused by the flow between the Taylor vortex and the large basic vortex. For $t \gtrsim 152\pi$ there is an inflow at approximately 0.8 gap widths caused by the pinched flow on the equatorial side of the stagnation point. The maximum radial velocity in figure 8 is 0.034.

Figure 9(*a*) shows that except for $140\pi < t < 165\pi$ the torque slowly decreases at the inner sphere. The sudden decrease for $140\pi < t < 152\pi$ is due to the disappearance of the Taylor-vortex pair which is a very efficient transporter of angular momentum. The sudden increase in τ_1 for $t > 152\pi$ coincides with the formation of the pinch which is also efficient in carrying momentum flux. Note that the timescales for the rapid change in τ_1 are of the order of σ/u_r (which is approximately $\frac{1}{4}$ the viscous diffusion time between the inner and outer spheres). If we consider the angular momentum flux of the Taylor vortex and of the pinch to be indicative of their strengths, then figure 9(*b*) shows that the Taylor vortex decreases in strength more rapidly in time at the outer boundary that it does at the inner boundary (i.e. $\tau_1 > \tau_2$ for $t < 152\pi$) and that the pinch grows in strength more rapidly at the outer boundary than it does at the inner boundary (i.e. $\tau_2 > \tau_1$ for most $t > 152\pi$).

3.3. $0 \rightarrow 1$ *transition*

We simulate the $0 \rightarrow 1$ transition by starting with the steady-state 0-vortex equilibrium at $Re = 650$. At $t = 0$ we then reduce the viscosity so that $Re = 700$ where the 0-vortex equilibria is unstable. Figure 10(*a*) shows the approximate equilibrium 0-vortex flow at $t = 60\pi$. Note that the flow is reflection-symmetric about the equator. Each hemisphere has a pinch in the large basic vortex; there are closed streamlines (approximately one gap width in diameter on the equatorial side of the stagnation point) whose circulation is of the same sign as the large basic vortex.

Before describing what does happen in the $0 \rightarrow 1$ transition let us first describe what does not happen. Suppose the flow in the small closed streamlines in the pinch broke off to become a Taylor vortex, as in the $0 \rightarrow 2$ transition of figure 4, but that this

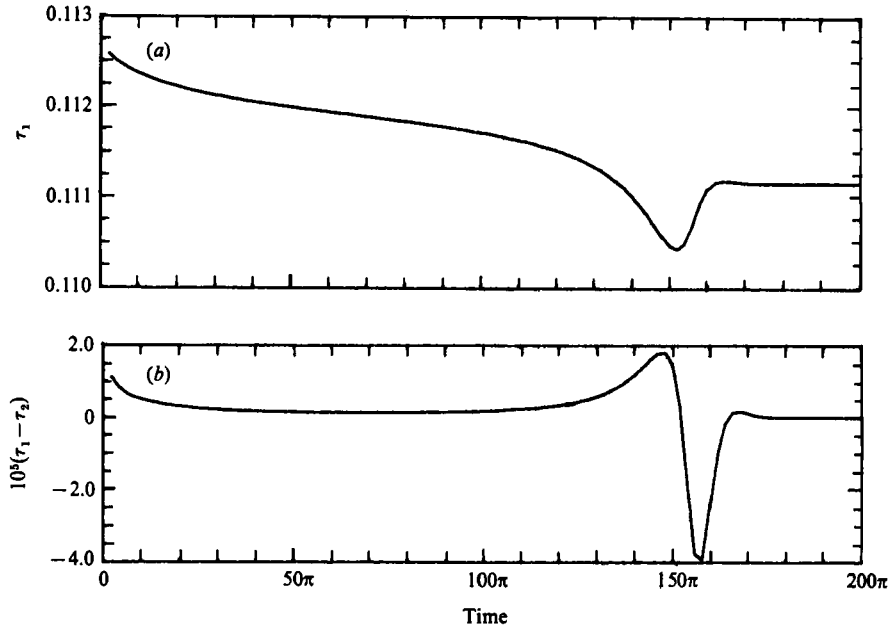

FIGURE 9. The torque τ_1 and the difference $(\tau_1-\tau_2)$ plotted as in figure 6 for the $1\rightarrow 0$ transition.

break were not accompanied by the formation of a second recirculating Taylor vortex. Then the circulation of the newborn Taylor vortex would have the wrong sign; the large basic vortex and the abutting Taylor vortex would be rotating in the same direction with a stagnation point between them, whereas neighbouring Taylor vortices always have opposite signs. Furthermore, a 1-vortex flow formed by pinching off the closed streamlines would have a radial outflow at the equator, but the observed 1-vortex flows have radial inflows at the equator. We conclude that the $0\rightarrow 1$ transition cannot occur by this type of pinching process.

An alternative scenario for the $0\rightarrow 1$ transition is the time-reverse of the $1\rightarrow 0$ transition shown in figure 7. If the $0\rightarrow 1$ transition occurred by this route, it would require the spontaneous creation of a pair of recirculating Taylor vortices at the outflow boundary at the equator. Although this creation is allowed kinematically, we note that in our study of Couette flows in spheres and in cylinders (Marcus 1984) we have never observed the spontaneous creation of a pair of Taylor vortices. The only times vortices are created is when one recirculating Taylor vortex (not a pair of vortices) forms at a stagnation point where the local Reynolds number is $O(10)$. (This observation is discussed further in §6.) In any case, the observed $0\rightarrow 1$ transition does not proceed as the time-reverse of the $1\rightarrow 0$ transition.

Instead, as figure 10 shows, the $0\rightarrow 1$ transition is asymmetric with respect to reflection about the equator. In the next section we shall show that the transition is due to a linear instability to an eigenmode that is antireflection-symmetric about the equator. Figure 10(*b*) shows the first observable appearance of asymmetry with the outflow boundary between the two large basic vortices moving below the equator. The 1-vortex flow begins in figure 10(*c*) when two wedge-shaped recirculating regions form near the stagnation point at the inner and outer boundaries at $\theta = 29\pi/64$. The local Reynolds number of the instability in figure 10(*c*) (based upon the gap width, ν, and the energy of the antireflection-symmetric component of the velocity) is $O(10)$.

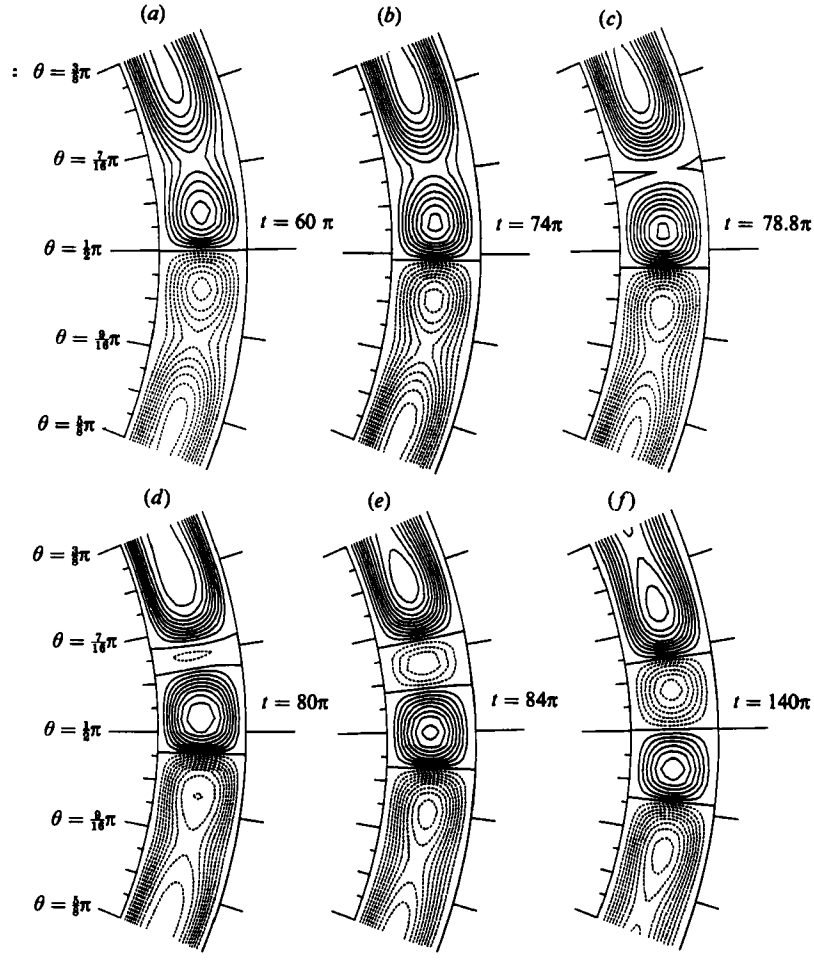

FIGURE 10. Meridional flow plotted as in figure 4 during the $0 \rightarrow 1$ transition at the six times indicated. The flows inside the two wedges at $\theta = \frac{39}{64}\pi$ in figure 10(*c*) are recirculating. If contours had been drawn for very low values of the streamfunction, there would be closed dashed streamlines inside the two wedges.

The two recirculating regions in figure 10(*c*) join together to form the recirculating Taylor vortex in figure 10(*d*). When the recirculating Taylor vortex forms, what was formerly the pinch in the northern hemisphere's large basic vortex becomes a separate Taylor vortex. This separate Taylor vortex moves south across the equator (figure 10*e*) and eventually becomes the Taylor vortex of the southern hemisphere in the equilibrium 1-vortex flow (figure 10*f*). The recirculating vortex that formed at the stagnation point in the northern hemisphere becomes the northern hemisphere's Taylor vortex. If the initial conditions are infinitesimally perturbed, the $0 \rightarrow 1$ transition can occur by forming a recirculation vortex in the southern hemisphere (see §4). The formation of the recirculation vortex in the $0 \rightarrow 1$ transition shown in figures 10(*c*) and 10(*d*) is essentially the same phenomenon that occurs in the $0 \rightarrow 2$ transition, but in the $0 \rightarrow 1$ transition the recirculation vortex forms only in one hemisphere.

The timescales in figure 10 are somewhat misleading. It takes approximately 10 inner sphere rotation periods for the transition from the equilibrium flow at $Re = 650$

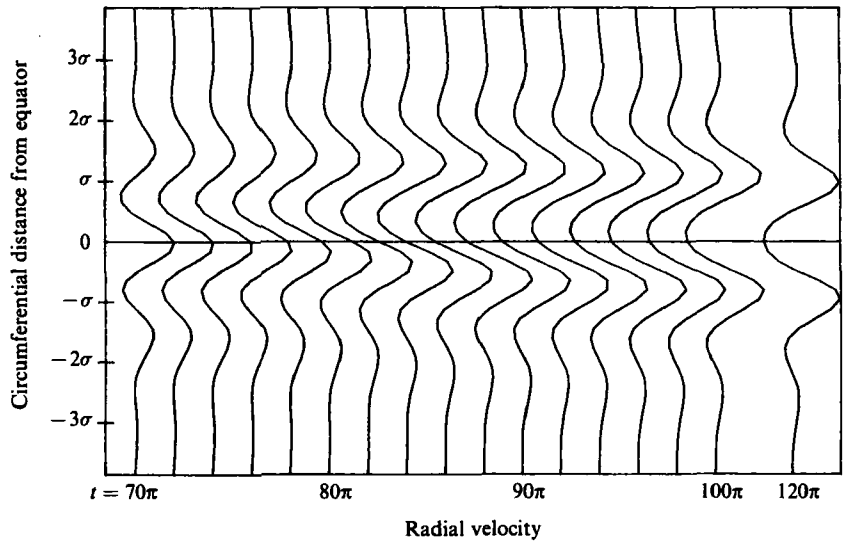

FIGURE 11. Radial velocity, plotted as in figure 5 during the $0 \rightarrow 1$ transition. The maximum radial velocity shown is 0.066. The entire velocity profile slides southward during the transition and changes the equator from an outflow to an inflow boundary.

to the (approximate) equilibrium flow at $Re = 700$. The subsequent timescales of the transition depend sensitively upon the amplitude spectrum of the initial perturbations, which in turn depends on background noise and transients caused by acceleration in laboratory experiments or on the round-off, truncation, aliasing, and timestepping errors in numerical experiments. The one timescale associated with $0 \rightarrow 1$ transition that does not depend on initial conditions is the growth rate λ of the linear instability to be discussed in §4.

We summarize the scenario for the $0 \rightarrow 1$ transition: (i) for $0 < t \leqslant 20\pi$ the flow adjusts slowly from the stable equilibrium at $Re = 650$ to the unstable (approximate) equilibrium at $Re = 700$, and during this adjustment the angular momentum gradient is not steep enough to cause a linear instability (note that in §4 we show that the linear instability is indeed due to an adverse angular momentum gradient). (ii) At $t \approx 20\pi$ the linear instability starts to grow as $e^{\lambda t}$. Approximately linear growth continues until the local Re exceeds $\mathcal{O}(10)$ where the local Re is based on the gap width, ν, and the velocity of the antisymmetric eigenmode (which is approximately the value of u_r at the latitude of the stagnation point). (iii) When the local $Re \geqslant \mathcal{O}(10)$, a recirculation vortex begins to form at the stagnation point. (iv) The recirculation vortex grows rapidly and nonlinearly to its final equilibrium strength and size in an advective timescale. (v) After this rapid growth the flow changes extremely slowly as it re-establishes reflection symmetry about the equator. The physics responsible for the long timescale associated with the decay of the antisymmetric part of the flow is discussed in §5.

From figure 10 (and figure 21 in §5) and from the assumption that the linear instability does not begin to grow until time $t = 20\pi$, we see that the lapse of time between the start of linear instability and the time that the local Re of the eigenmode is $\mathcal{O}(10)$ (i.e. a dimensionless radial velocity of 0.0794), is approximately 60π. A linear growth rate of $\lambda = 0.071$ (see figure 16 in §4) implies that the initial amplitude of our unstable velocity eigenmode (in dimensionless units) is approximately 10^{-7}. This

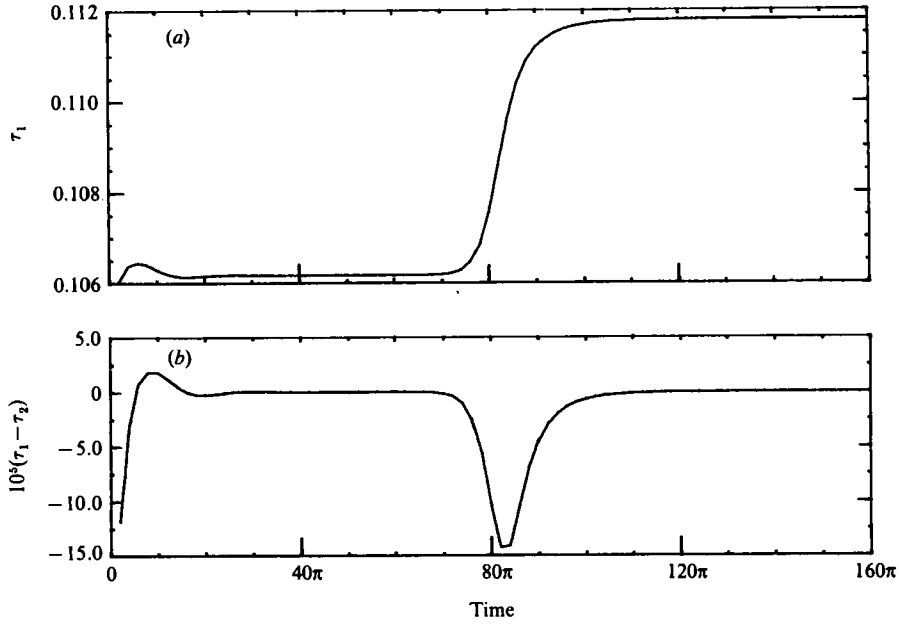

FIGURE 12. τ_1 and $(\tau_1-\tau_2)$ plotted as in figure 6 for the $0\rightarrow 1$ transition. The length of time between $t=0$ and the sudden change in τ_1 and $(\tau_1-\tau_2)$ at $t=70\pi$ is a function of the initial amplitude of the unstable eigenmode.

amplitude is consistent with the numerical round-off and aliasing errors produced by our code.

Several of the laboratory observations (or lack thereof) of the $0\rightarrow 1$ and $0\rightarrow 2$ transitions can be explained by the slow timescale of the linear instability. Wimmer's experimental findings are consistent with our numerical result: if one increases the Reynolds number by accelerating the inner sphere from the rest slowly (of the order of, or longer than the timescale associated with the linear instability) then there must be a $0\rightarrow 1$ transition.

The $0\rightarrow 2$ transition occurs when the acceleration is quick but sufficiently smooth so that the flow is allowed to pass through a series of quasi-equilibria that closely follow the 0- and 2-vortex equilibrium curve. The passage through the unstable portion at $651 \leqslant Re \leqslant 775$ must be fast with respect to the growth time of the linear instability.

The spontaneous symmetry breaking in the $0\rightarrow 1$ transition is shown clearly in figure 11. The radial outflow boundary at the equator in the 0-vortex flow appears in figure 11 as the outward bulge at the equator at $t=70\pi$. The bulge moves downward across the equator throughout the transition, and at $t=120\pi$ represents the outflow boundary between the recirculation Taylor vortex and the large basic vortex of the southern hemisphere. The radial inflow at 0.8σ north of the equator is initially due to the flow in the pinch on the equatorial side of the stagnation point. During the transition it moves southward and it eventually becomes the radial inflow boundary at the equator. The maximum radial velocity in figure 11 is 0.066.

Figure 12(a,b) shows an initial bump and overshoot in τ_1 and $(\tau_1-\tau_2)$. These features are characteristics of the abrupt increase in Re at $t=0$ and are not associated with the $0\rightarrow 1$ transition. The long flat features of τ_1 and $(\tau_1-\tau_2)$ at

$15\pi < t < 70\pi$ are the slow settling of the flow into the unstable 0-vortex equilibrium at $Re = 700$. The abrupt change near $t = 80\pi$ happens on the timescale of the linear instability, $1/\lambda \approx 5\pi$ (see figure 16). During this time the inner torque increases monotonically to nearly its final value, and the recirculation vortex forms. The torque is relatively insensitive to the re-establishment of reflection-symmetry at $t > 90\pi$; angular momentum is transported by the vortices regardless of their position relative to the equator. Figure 12(*b*) can be interpreted as showing that the angular momentum flux carried by the recirculation vortex grows initially at the outer boundary (i.e. for $70\pi < t < 82\pi$, $\tau_2 > \tau_1$) and at later times, $t > 82\pi$, the angular momentum flux at the inner catches up to the flux at the outer boundary.

3.4. $2 \rightarrow 1$ *transition*

The 2- to 1-vortex transition is also asymmetric with respect to the equator. This transition has not received nearly as much attention as the $0 \rightarrow 1$ transition, and in fact, has never been mentioned in either the published numerical or experimental literature. (Experimental evidence for its existence has been communicated to us privately by K. Bühler 1983.) The absence of the $2 \rightarrow 1$ vortex transition in the numerical literature can be explained easily by its asymmetry. The lack of mention in the experimental literature could be due to the fact that this transition occurs only in a small range of Reynolds number $740 < Re < 775$, and like the $0 \rightarrow 1$ transition, slow changes in the Re are needed for this transition to occur (see below).

We speculate, in the same way as we did for the $0 \rightarrow 1$ vortex transition, how a $2 \rightarrow 1$ transition could take place symmetrically. It would not suffice for the two small recirculating Taylor vortices in figure 13(*a*) at $\pm\sigma$ from the equator to disappear, since not only would this cause vortices of the same sign to abut each other but also the resulting 1-vortex flow would have a radial outflow boundary at the equator which would be incorrect. Alternatively, a pair of Taylor vortices could be destroyed at the equator. This type of transition is allowed kinematically and results in a 1-vortex flow with the correct appearance. However, we note that whenever we have seen a Taylor-vortex pair disappear in our numerical experiments, the two vortices are recirculating and are joined together at an inflow boundary (e.g. the $1 \rightarrow 0$ transition in figure 7). To produce the $2 \rightarrow 1$ transition would require destroying a pair of strong non-recirculating vortices connected at an outflow boundary.

Figure 13 shows the time evolution of the meridional velocity during our numerically simulated $2 \rightarrow 1$ transition. The transition is produced by starting with the steady-state 2-vortex equilibrium at $Re = 800$. At $t = 0$ the viscosity is reduced so that $Re = 750$, and the 2-vortex flow is linearly unstable. The $2 \rightarrow 1$ transition is similar in many ways to the $0 \rightarrow 1$ transition. From $t = 0$ to $t = 100\pi$ the flow slowly evolves into the approximate unstable 2-vortex equilibrium at $Re = 750$ (figure 13*a*). (Starting the flow at $t = 100\pi$ with the exact unstable $Re = 750$ equilibrium does not qualitatively change our results.) The recirculating Taylor vortices in figure 13(*a*) are narrow; their circumferential extent is less than $\frac{1}{4}$ of the gap width.

As the instability progresses, the recirculating Taylor vortex in the southern hemisphere shrinks, and the equatorial outflow boundary moves southward (figure 13*b*). Unlike those in steady-state equilibria, the vortex boundaries in figure 13(*b*) are not straight radial lines. At $t = 116\pi$ the southern recirculation vortex disappears and leaves two recirculating wedges. Between the wedges a stagnation point forms (figure 13*d*) allowing the fluid that was in the original southern large basic and non-recirculating Taylor vortices to merge together to form a single pinched large basic vortex. The recirculation vortex in the northern hemisphere grows in size and

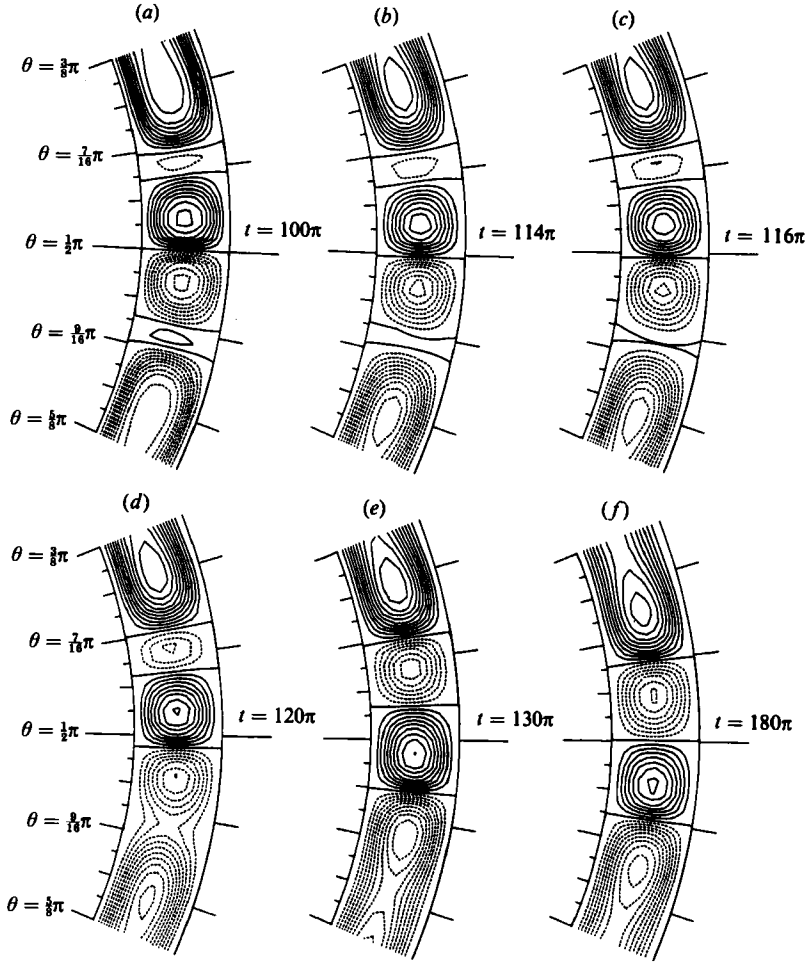

FIGURE 13. Meridional flow plotted as in figure 4 during the $2 \rightarrow 1$ transition. The flows in between the two solid streamlines at $\theta = \frac{35}{64}\pi$ in (*b*) and the two wedges at the same latitude in (*c*) are recirculating. Additional contours would show that the flow in these regions would consist of solid closed contours.

strength (figure 13*e*) and moves southward where its southern boundary eventually forms the radial outflow of the equator (figure 13f). Equatorial symmetry is re-established by $t = 180\pi$.

The radial velocity profiles in figure 14 are similar to those in figure 11. The radial inflows and outflows slide southward during the transition, causing the equator to change from an outflow to an inflow boundary. One reason that the $2 \rightarrow 1$ transition appears so smooth and continuous in figure 14 is that the profiles of $u_r(r = \bar{r}, \theta, t)$ cannot distinguish between flows that are pinched with stagnation points and flows with recirculating Taylor vortices. The maximum value of u_r in figure 14 is 0.078.

Figure 15(*a*) shows the torque at the inner boundary adjust initially to the appropriate value for the 2-vortex unstable equilibrium at $Re = 750$. The torque changes abruptly from $t \approx 120\pi$ to 125π. Note that 5π is the approximate timescale of the linear instability (see §4). The fact that the abrupt change occurs at $t \approx 120\pi$ is due only to the initial amplitude of the linearly unstable eigenmode. If the amplitude were greater, the transition would occur earlier.

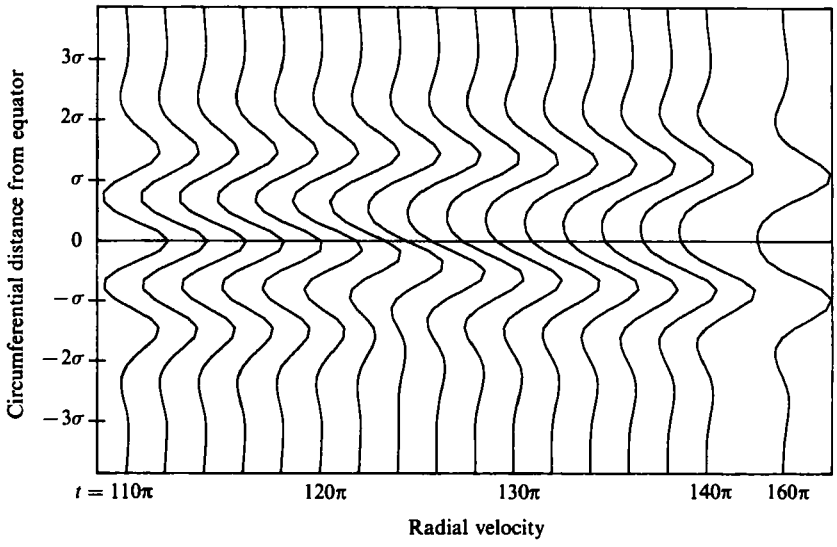

FIGURE 14. Radial velocity plotted as in figure 5 for the $2 \rightarrow 1$ transition. The maximum velocity shown in 0.078.

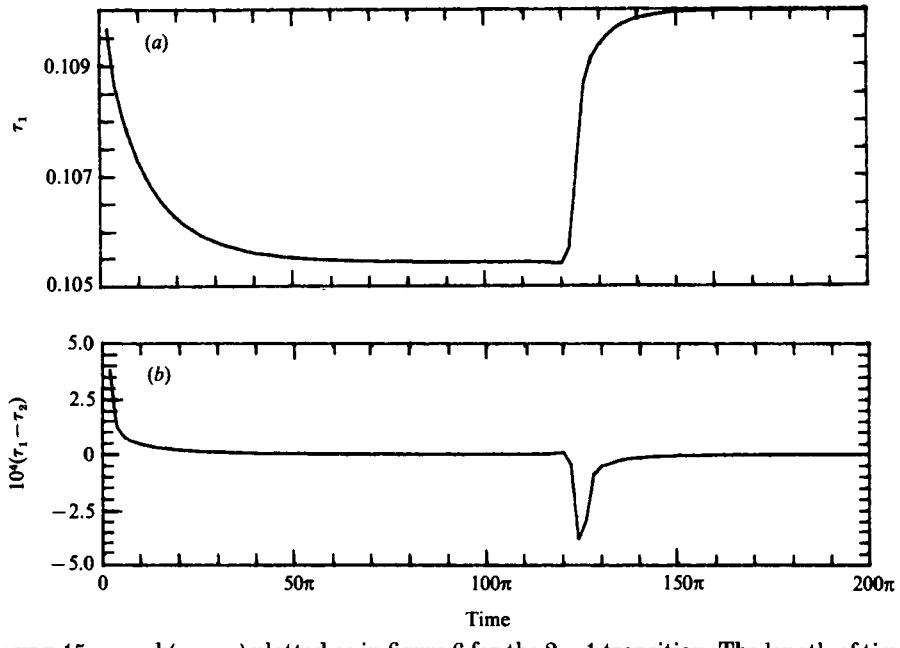

FIGURE 15. τ_1 and $(\tau_1 - \tau_2)$ plotted as in figure 6 for the $2 \rightarrow 1$ transition. The length of time between $t = 0$ and $t = 120\pi$ where there is a sudden change in τ_1 and $(\tau_1 - \tau_2)$ is a function of the initial amplitude of the unstable eigenmode.

Figure 15(*a*) shows that the abrupt changes in τ_1 do not begin until after $t = 120\pi$ which indicates that the angular momentum flux is not greatly affected by the disappearance of the recirculating vortex in the southern hemisphere at $t = 116\pi$; recirculation vortices and pinches with stagnation points carry roughly the same angular momentum flux. It is the abrupt increase in size and strength of the

recirculation vortex of the northern hemisphere at $t = 120\pi$ that causes τ_1 to increase. The temporal evolution for $(\tau_1 - \tau_2)$ shown in figure 15(*b*) is similar to the curve in figure 12(*b*). The initial rapid adjustment at $t = 0$ has opposite signs in these two figures because the transition in figure 12(*b*) is caused by decreasing *Re*. The downward dip in $(\tau_1 - \tau_2)$ at $t = 124\pi$ can be interpreted as the northern recirculation vortex increasing in strength first at the outer boundary and then later catching up at the inner boundary.

4. Linear eigenmodes

Using the numerical methods described in Part 1 we have computed the unstable 0- and 2-vortex equilibria and calculated the eigenmodes to which they are unstable and the corresponding eigenvalues. We have found that the 0- and 2-vortex equilibrium curve shown in figure 1 is unstable for $651 < Re < 775$ to eigenmodes that are antireflection-symmetric with respect to the equator and that the eigenvalue of the most unstable or least stable eigenmode is always real. The neutral stability that we find at $Re = 652$ agrees with Wimmer's experimental results (private communication, 1983) to three significant digits and that at $Re = 775$ agrees with Bühler's experiments (private communication, 1983). Our numerical results show that the entire 0- and 2-vortex equilibrium curve is stable with respect to reflection-symmetric eigenmodes for all $Re < 1300$ (the extent of our numerical experiments).

Since the Navier–Stokes equation, the boundary conditions for spherical Couette flow, and the nonlinear 0- and 2-vortex equilibria are all reflection-symmetric about the equator, the linear eigenmodes of these equilibria must have a definite parity and be either reflection- or antireflection-symmetric. Asymmetric eigenvectors (of neither parity) must be the sum of two (or more) eigenvectors of opposite parity and can occur only if there is an accidental degeneracy of two (or more) eigenvalues. Yakushin, in his study of the Stokes flow with narrow-gap widths found that the eigenfunctions occur as nearly degenerate pairs, with the growth rates of the antisymmetric and symmetric eigenmodes intertwined (1969). Blennerhassett & Hall found the same result for low *Re* Taylor–Couette flow with finite cylinders (1979).

Our numerically computed eigenvalue λ of the most unstable eigenmode of the 0- and 2-vortex equilibria as a function of *Re* is shown in figure 16 as the heavy solid curve. Because the curve is continuous at $Re = 740$ (where the $0 \rightarrow 2$ transition defined by the formation of recirculation vortices occurs), we conclude that the eigenmodes responsible for the $0 \rightarrow 1$ and the $2 \rightarrow 1$ transition are part of the same family (see below). The growth rate λ reaches its maximum value at $Re = 735$ (not $Re = 740$). $Re = 735$ corresponds to the minimum of the torque along the 0- and 2-vortex equilibrium shown in figure 1. From this, we conjecture that the linear instability is due to the inability of the 0- and 2-vortex flows to effectively transport angular momentum.

One way of determining whether the linear instability of the 0-vortex flow is due to the adverse angular momentum gradient of the azimuthal flow or due to the stagnation point of the meridional flow is to consider the linear instabilities of Stokes flow which is purely azimuthal with no meridional circulation. The Stokes flow, $\boldsymbol{u}^*$ is not an equilibrium solution, but nonetheless one can still formally define a $\boldsymbol{u}'(r, \theta, t)$ such that

$$\frac{\partial \boldsymbol{u}'}{\partial t} = -\boldsymbol{u}^* \cdot \nabla \boldsymbol{u}' - \boldsymbol{u}' \cdot \nabla \boldsymbol{u}^* - \nabla P' + \frac{1}{Re} \nabla^2 \boldsymbol{u}'. \tag{4.1}$$

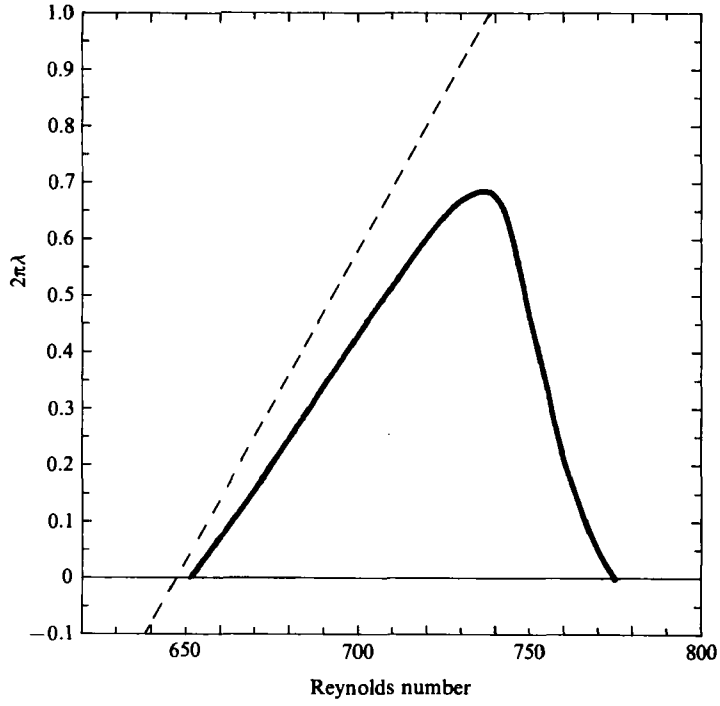

FIGURE 16. The growth rate λ of the most unstable eigenmode of ——, the 0- and 2-vortex equilibria, and of – – –, the Stokes flow. The dashed curve increases monotonically with Re, but the solid curve turns over at $Re = 735$ as the equilibrium flow become more efficient at transporting angular momentum away from the inner sphere.

The growth rates of the most unstable (or least stable) eigenmodes of the Stokes flow are shown in figure 16 as the dashed line. The dashed and solid curves are very close for $Re < 700$. In particular, the Re for neutral stability is 648 for Stokes flow and 652 for the true 0-vortex flow. We note that for $Re < 700$ the azimuthal component of the 0-vortex flow's and the Stokes flow's velocity are not very different, but that for $Re > 700$ the two velocities differ substantially due to the transport of angular momentum by the meridional flow (see Part 1). The good agreement between the solid and dashed curves for $Re < 700$ indicates that linear stability depends much more strongly on the azimuthal than on the meridional flow. The meridional part of the basic flow with its stagnation points and pinches does not play an important role in the onset of instability; the linear instability of spherical Couette flow is driven by an adverse angular momentum gradient as is the linear instability of circular Couette flow in infinite cylinders.

Because the Stokes flow has no meridional transport of angular momentum, the adverse angular momentum gradient continues to grow with Re and the growth rate shown by the dashed curve in figure 16 increases monotonically with Re. The neutrally stable point of the true flow at $Re = 775$ cannot be predicted by the study of eigenvalues of Stokes flow (cf. Yakushin 1969).

The similarities and differences between the eigenmodes of the Stokes and of the 0- and 2-vortex flows is best shown in the plots of the eigenvectors. Figure 17 (a–c) shows the meridional streamfunction, the contours of constant azimuthal angular velocity, and the energy spectrum of the unstable eigenvector of Stokes flow at $Re = 700$. The eigenvector is composed of alternating Taylor vortices with the vortex

boundaries (inflow or outflow) appearing as solid radial streamlines in figure 17(*a*). The velocity is manifestly antisymmetric – there is flow across the equator which is forbidden in symmetric flows. The surfaces of constant azimuthal angular velocity are shown in figure 7(*b*). Despite the similarity between figures 17(*a*) and 17(*b*) they represent entirely different aspects of the flow. In figure 17(*a*) the meridional component of the velocity is along the closed contours. In figure 17(*b*) the azimuthal flow is perpendicular to the closed contours – into the page at the broken curves and outward from the page at the solid curves. Surfaces of constant angular velocity in Stokes flow are independent of θ. The azimuthal velocity of the eigenmode alternates in direction as a function of θ and has its amplitude maxima near the Taylor-vortex boundaries shown in figure 17(*a*). The solid straight radial lines in figure 17(*b*) are the contours of zero azimuthal velocity and are near the Taylor-vortex centres. In parts of the flow not shown, i.e. $\theta > \frac{5}{8}\pi$ and $\theta < \frac{3}{8}\pi$ the Taylor-vortex structure continues with the same periodicity but becomes progressively weaker as the poles are approached.

The energy spectrum of the eigenfunction in figure 17(*c*) is plotted as a function of vector spherical harmonic number L as in Part 1. For an antisymmetric velocity the meridional velocity spectrum exists only at odd values of L and the azimuthal spectrum at even values and vice versa for reflection-symmetric flows. The continuous curves, (solid for azimuthal and dashed for meridional) in figure 17(*c*) are drawn through the 32 ± 1 points of the discrete spectra. The spectra show that eigenmode of the Stokes flow have more energy in their azimuthal than in their meridional components. This is also a property of the linear eigenmodes that produce the Taylor vortices in circular Couette flow in infinite cylinders (Marcus 1984). The maximum amplitude in the spectrum is at $L = 24$ and corresponds to $\Delta\theta \simeq 0.083\pi$, where $\Delta \equiv 2\pi/L$. The angular size corresponds to the latitudinal extent of a Taylor-vortex pair (which is somewhat less than twice the gap width) shown in figure 17(*a*).

The unstable eigenmodes of the 0-vortex flow at $Re = 700$ and of the 2-vortex flow at 750 are shown in figures 18 and 19 respectively. (For the meridional and azimuthal velocities and energy spectra of 0- and 2-vortex equilibrium flows see Part 1.) The eigenfunctions in figures 18 and 19 are similar to each other and to the eigenfunction of the Stokes flow in figure 17, confirming our conjecture that the instabilities of the 0- and 2-vortex flows are both due to the azimuthal flow. Figures 18 and 19 show that the instability of 0- and 2-vortex flow is more concentrated at the equator, than it is for the Stokes flow.

The contours of zero azimuthal velocity of the eigenfunction of the Stokes flow shown in figure 17(*b*) are straight radial lines. In the eigenfunctions of 0- and 2-vortex flows these contours become very distorted as shown in figures 18(*b*) and 19(*b*). However, these curved contours of the eigenfunction are nearly perpendicular to the contours of constant azimuthal angular velocity of the unstable equilibria. This property is illustrated in figure 20(*a–c*) where we have plotted the contours of constant angular velocity (thin solid lines) of the Stokes (*a*), 0-vortex (*b*), and 2-vortex (*c*) flows. Superposed on these figures are the contours of zero azimuthal velocity of their respective unstable eigenfunctions (thick solid curves). Note that although figures 20(*b*) and 20(*c*) represent the 0- and 2-vortex flows respectively, the azimuthal velocities of the two flows are qualitatively similar.

We conclude this section by noting that the knowledge of the linearly unstable eigenfunctions of 0- or 2-vortex flows sheds no light at all on the nonlinear evolution of the flow initiated by these instabilities or on the flow's eventual steady-state

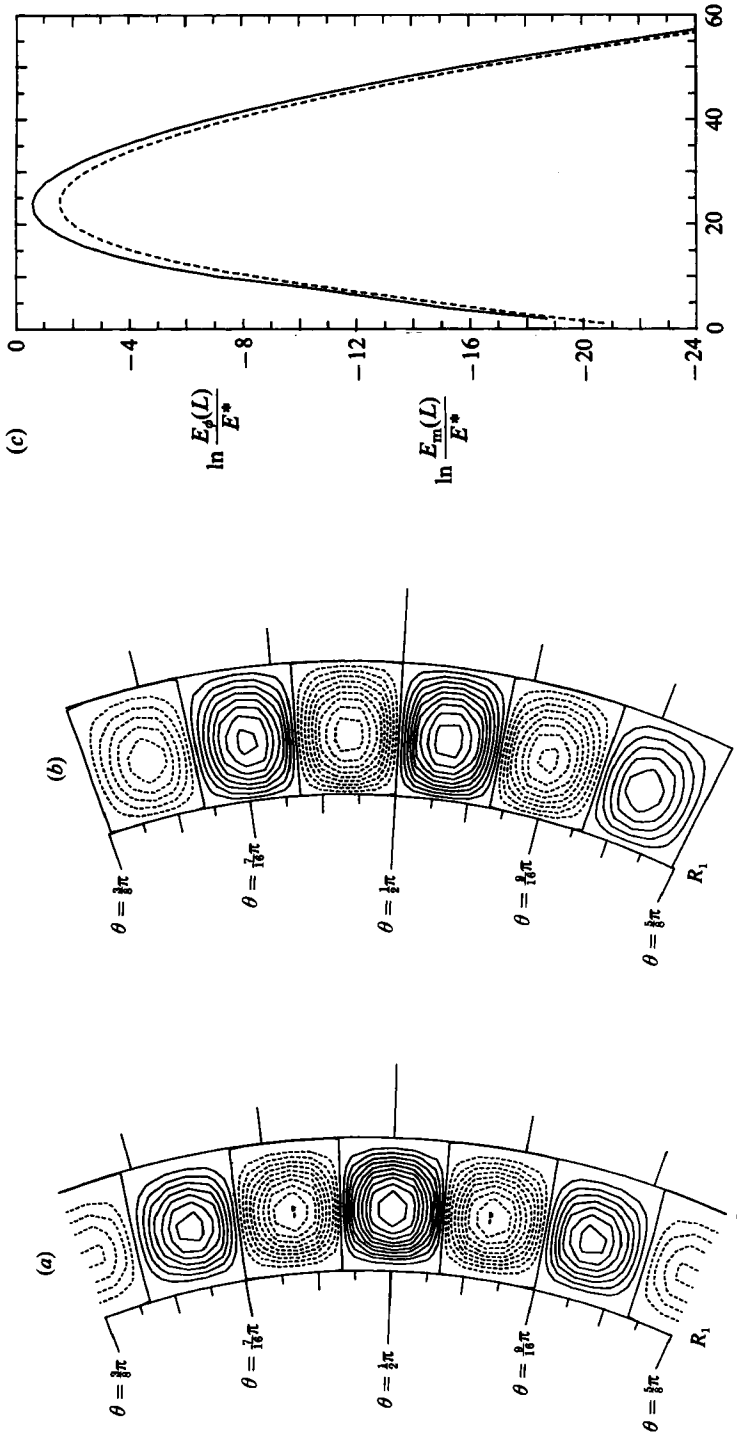

FIGURE 17. The antireflection-symmetric unstable eigenfunction of the Stokes flow at $Re = 700$ (*a*) meridional streamlines, (*b*) contours of constant azimuthal angular velocity, and (*c*) energy spectra. The meridional streamlines are plotted with the same conventions used in figure 4. The solid (dashed) curves in (*b*) represent azimuthal velocity coming out of (going into) the page. The solid radial curves in (*b*) extending from the inner to the outer boundaries are the contours of zero azimuthal velocity. The energy spectra are a function of the vector harmonic number L defined in Part 1. The solid (dashed) curve is for the azimuthal (meridional) component of the velocity and exists only at even (odd) values of L. The unit of energy in (*c*) is E^*, which is the energy of the Stokes flow with the same Re and σ.

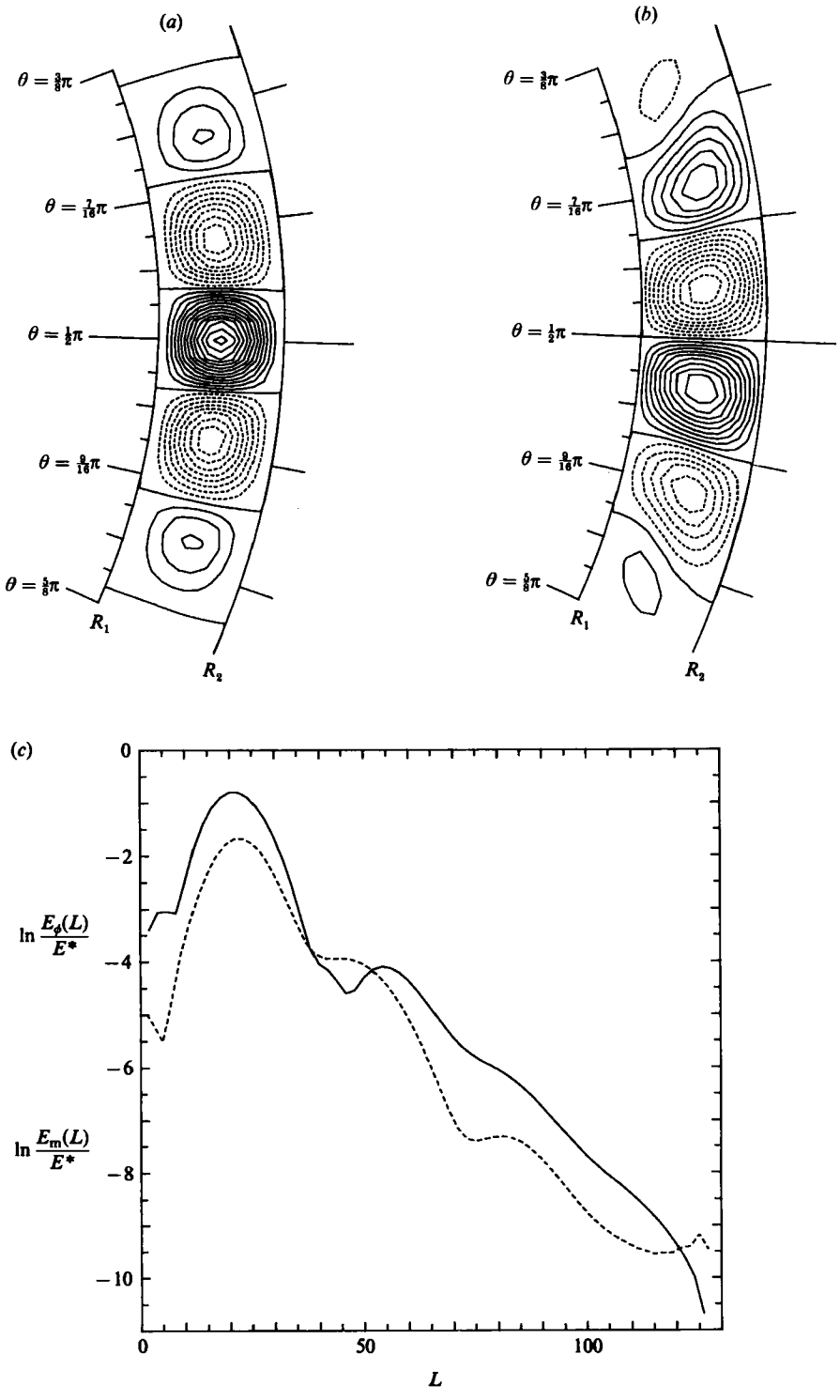

FIGURE 18. The unstable eigenmode of the 0-vortex flow at $Re = 700$ plotted as in figure 17.

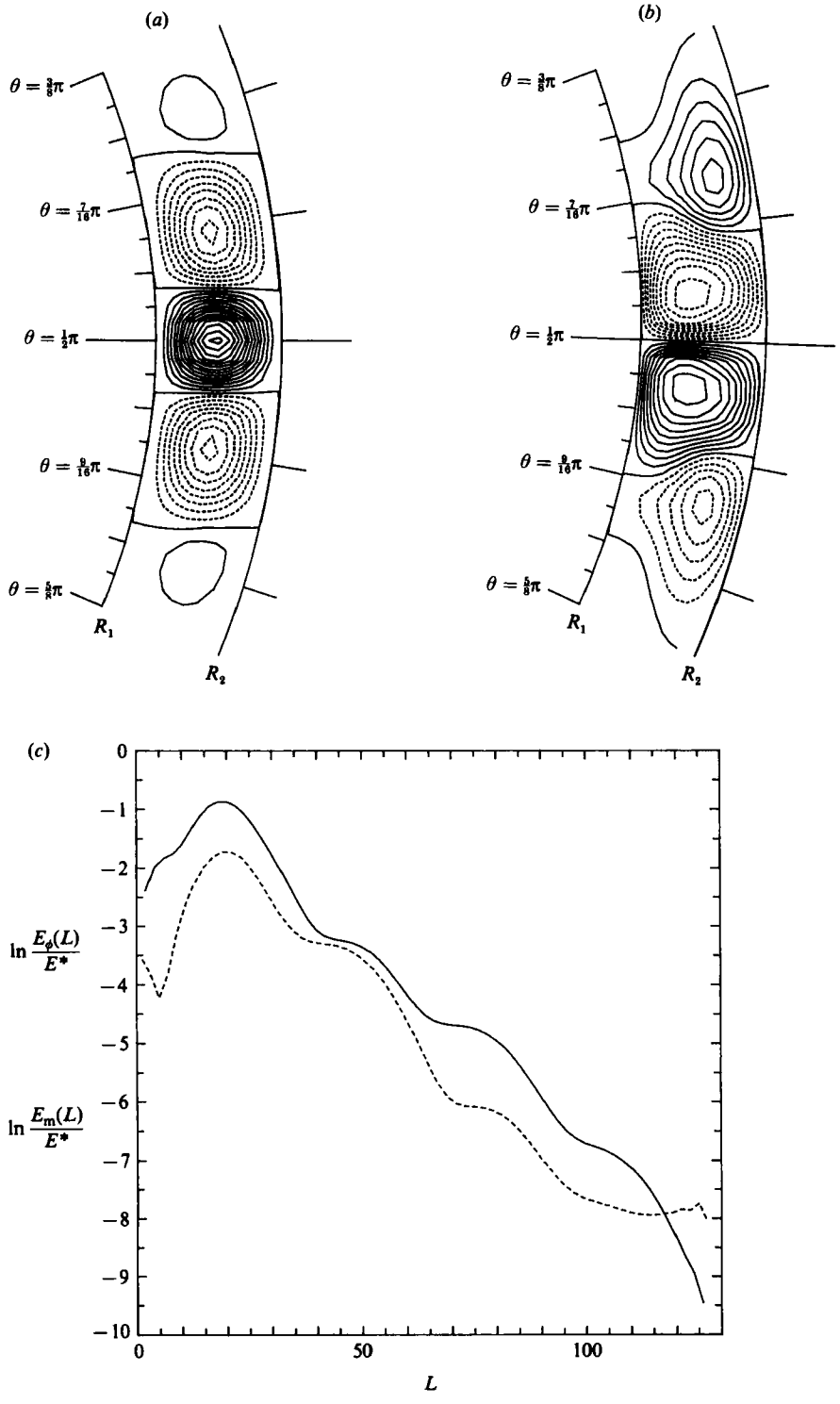

FIGURE 19. The unstable eigenmode of the 2-vortex flow at $Re = 750$ plotted as in figure 17.

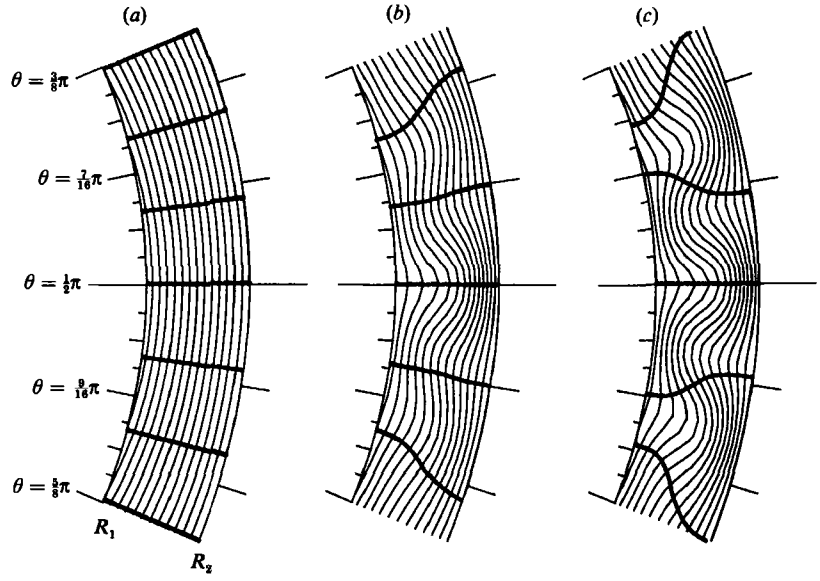

FIGURE 20. The constant contours of the azimuthal angular velocity (thin solid curves) of equilibrium (*a*) Stokes flow at $Re = 700$, (*b*) 0-vortex flow at $Re = 700$, and (*c*) 2-vortex flow at $Re = 750$, superposed with the contours of zero azimuthal velocity of the corresponding unstable eigenmodes (thick solid curves).

destination. To determine the final equilibria it is necessary to have knowledge of global information such as the bifurcation diagram in figure 1. Using figure 1 we know that a linear instability of the 0- and 2-vortex flows at $651 < Re < 775$ must result eventually in the 1-vortex flow (provided there are no stable equilibria missing from the figure). The drawback of a linear stability analysis becomes evident when we compare our results to the stability analyses of Yakushin (1969), Munson & Joseph (1971) and Munson & Menguturk (1975). These authors found that the eigenvectors with the lowest critical Reynolds number were antisymmetric (like our eigenmodes). They therefore suggested that the final equilibrium steady states would be asymmetric, in contradiction to the observed reflection-symmetric 1-vortex flow.

5. Energy transfer

One way of studying the $0 \rightarrow 1$ or $2 \rightarrow 1$ transitions when they become nonlinear is to examine the energy transfer among different modes. Considering the fact that these transitions begin and end with reflection-symmetric flows, yet are initiated by antireflection-symmetric eigenmodes, it is most useful to examine the energy transfer between the reflection-symmetric and antireflection-symmetric components of the velocity. We separate the Navier–Stokes equation into two components:

$$\frac{\partial \boldsymbol{u}_{\mathrm{R}}}{\partial t} = -(\boldsymbol{u}_{\mathrm{R}} \cdot \nabla)\,\boldsymbol{u}_{\mathrm{R}} - (\boldsymbol{u}_{\mathrm{A}} \cdot \nabla)\,\boldsymbol{u}_{\mathrm{A}} - \nabla P_{\mathrm{R}} + \frac{1}{Re}\nabla^2 \boldsymbol{u}_{\mathrm{R}}, \tag{5.1}$$

$$\frac{\partial \boldsymbol{u}_{\mathrm{A}}}{\partial t} = -(\boldsymbol{u}_{\mathrm{R}} \cdot \nabla)\,\boldsymbol{u}_{\mathrm{A}} - (\boldsymbol{u}_{\mathrm{A}} \cdot \nabla)\,\boldsymbol{u}_{\mathrm{R}} - \nabla P_{\mathrm{A}} + \frac{1}{Re}\nabla^2 \boldsymbol{u}_{\mathrm{A}}, \tag{5.2}$$

where

$$\boldsymbol{u} = \boldsymbol{u}_{\mathrm{R}} + \boldsymbol{u}_{\mathrm{A}}, \tag{5.3}$$

and where the A subscript means antisymmetric and R means reflection-symmetric component. Taking the dot products of (5.1) and (5.2) with their respective velocities and integrating over the entire domain of the fluid, we obtain

$$\frac{\partial E_{\mathrm{R}}}{\partial t} = -\dot{E}_{\mathrm{T}} - D_{\mathrm{R}} + \dot{E}_{\mathrm{IN}}, \tag{5.4}$$

$$\frac{\partial E_{\mathrm{A}}}{\partial t} = \dot{E}_{\mathrm{T}} - D_{\mathrm{A}}, \tag{5.5}$$

where E_{R} and E_{A} are the respective components of the kinetic energy of the fluid, $\dot{E}_{\mathrm{IN}}$ is the (necessarily reflection-symmetric) energy input rate due to the external torque driving the inner rotating sphere

$$\dot{E}_{\mathrm{IN}} \equiv \tau_1 \text{ (in dimensionless units)}, \tag{5.6}$$

D_{R} is the symmetric component of the viscous dissipation

$$D_{\mathrm{R}} \equiv \frac{1}{Re}\left(\tfrac{16}{3}\pi + \int (\nabla \times \boldsymbol{u}_{\mathrm{R}})^2 \, \mathrm{d}^3x\right) \geqslant 0, \tag{5.7}$$

D_{A} is the antisymmetric viscous dissipation

$$D_{\mathrm{A}} \equiv \frac{1}{Re} \int (\nabla \times \boldsymbol{u}_{\mathrm{A}})^2 \, \mathrm{d}^3x \geqslant 0, \tag{5.8}$$

and $\dot{E}_{\mathrm{T}}$ is the energy transfer function

$$\dot{E}_{\mathrm{T}} \equiv \int \boldsymbol{u}_{\mathrm{A}} \cdot [\boldsymbol{u}_{\mathrm{R}} \times (\nabla \times \boldsymbol{u}_{\mathrm{A}})] \, \mathrm{d}^3x, \tag{5.9}$$

and measures the rate of nonlinear energy transfer from the symmetric to the antisymmetric part of the flow. Note that the total energy E is $E_{\mathrm{R}} + E_{\mathrm{A}}$ because the cross-terms $\boldsymbol{u}_{\mathrm{A}} \cdot \boldsymbol{u}_{\mathrm{R}}$ and $\boldsymbol{u}_{\mathrm{R}} \cdot \boldsymbol{u}_{\mathrm{A}}$ vanish upon integration over the volume.

A number of properties of spherical Couette becomes apparent from (5.1)–(5.9). For example: (i) Although there can be symmetric and asymmetric equilibria, there can be no purely antisymmetric equilibria since (5.5) shows that with $\dot{E}_{\mathrm{T}} = 0$ it would be viscously dissipated. (ii) In an initial-value experiment (either in the laboratory or with the computer) a purely reflection-symmetric flow remains so indefinitely unless an antisymmetric perturbation is explicitly introduced, since (5.4) shows that the energy source for E_{A} is $\dot{E}_{\mathrm{T}}$, which is proportional to $\boldsymbol{u}_{\mathrm{A}}$.

Figure 21 shows the symmetric (long-dashed curve), the antisymmetric (short-dashed curve), and the total (solid curve) energy as a function of time during the $0 \rightarrow 1$ transition described in §3. The scale for the symmetric and total energy is given on the left-hand axis in units of the energy of the Stokes flow at $Re = 700$. The scale for the antisymmetric energy (which is much smaller than the symmetric energy) is on the right axis. The units between tick marks on the two axes are the same, but the origin on the right has been shifted so that all of the energies can be plotted on the same figure and so that the sum of the short- and long-dashed curves are equal to the solid curve.

The antisymmetric energy is initially zero, grows to a maximum value of 0.0105, and decreases again to zero. The symmetric energy decreases sharply, then increases. Its final 1-vortex state value is 0.999, less than the initial 2-vortex state value of

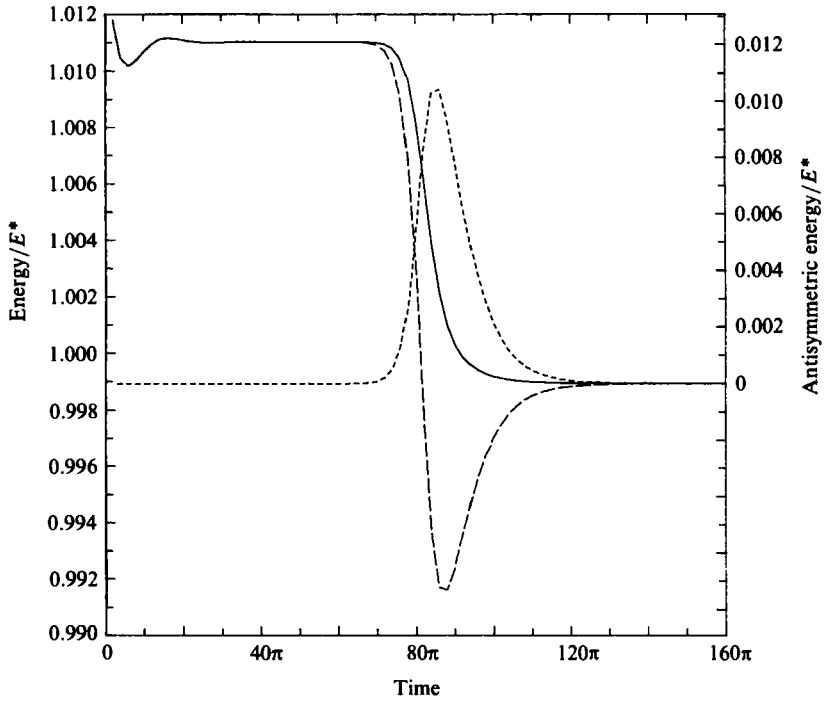

FIGURE 21. ———, symmetric, – – –, antisymmetric and ——, total energy during the $0 \rightarrow 1$ transition at $Re = 700$. The scale for the symmetric and total energy on the left-hand axis and the scale for the antisymmetric energy on the right-hand axis are the same, but the origins are different. The solid curve is equal to the sum of the two dashed curves.

1.011. The total energy decreases monotonically from 1.011 to 0.999. The increase in antisymmetric energy at the beginning of the transition mirrors the decrease in symmetric energy and vice versa at the end of the transition. This suggests the hypothesis that: (i) energy is transferred from the symmetric to the antisymmetric modes at onset of the transition and (ii) from the antisymmetric to the symmetric modes as symmetry is re-established. This hypothesis is false. We show this by plotting $\dot{E}_T$ in figure 22. We see that the first part of our hypothesis was correct: For $0 < t < 86\pi$ when $\dot{E}_A > 0$ figure 22 shows that $\dot{E}_T > 0$. This result is not surprising since the only energy source available to the antisymmetric flow is $\dot{E}_T$. However, the second part of our hypothesis is incorrect because when $\dot{E}_A < 0$, figure 22 shows that $\dot{E}_T$ is still greater than zero. In fact, $\dot{E}_T$ is always positive, and energy is never transferred from the antisymmetric to the symmetric part of the flow throughout the entire $0 \rightarrow 1$ transition (despite the fact that $\dot{E}_T$ is allowed kinematically to be negative).

How then does the antisymmetric velocity decrease? From (5.5), we see that $\dot{E}_A$ is the difference between $\dot{E}_T$ and D_A. Throughout the transition, $\dot{E}_T \approx D_A$ (the curves could not be distinguished from each other if both were plotted in figure 22). $\dot{E}_A$ is always the difference of two much larger numbers:

$$|\dot{E}_A| = |\dot{E}_T - D_A| \ll \dot{E}_T \approx D_A. \tag{5.10}$$

During the transition, the $\boldsymbol{u}_R$ and $\boldsymbol{u}_A$ velocities change such that $\dot{E}_T$ becomes less than D_A. At the beginning of the transition, E_A grows because $\dot{E}_T$ is large and is slightly greater than D_A; at the end E_A decays because $\dot{E}_T$ is large but is slightly less than

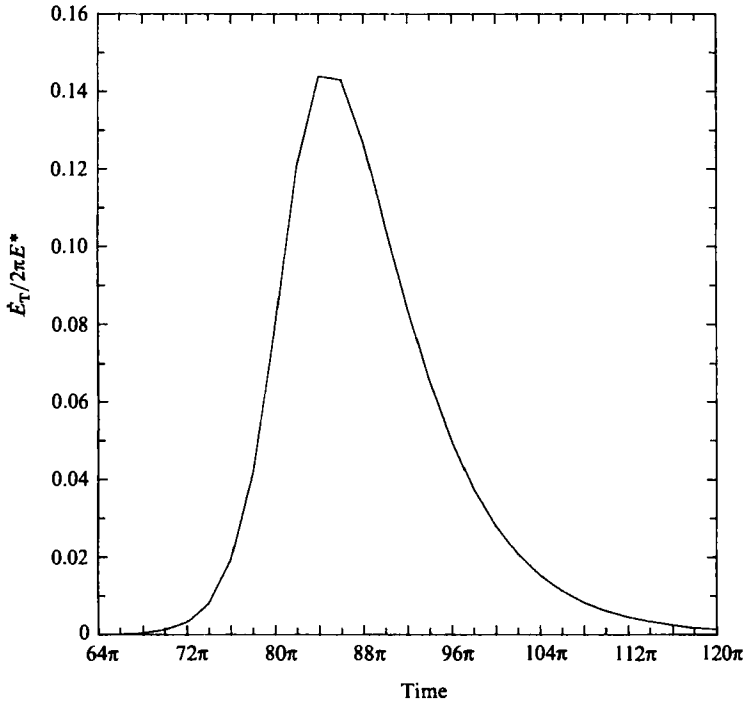

FIGURE 22. $\dot{E}_T$, the nonlinear transfer rate of energy from the symmetric to the antisymmetric part of velocity during the $0 \to 1$ transition shown in figure 21.

D_A. Figure 22 also explains the slow re-establishment of reflection-symmetry at the enc of the $0 \to 1$ transition; the antisymmetric component of the velocity decays on a timescale of order $E_A/|\dot{E}_T - D_A|$ which is much longer than E_A/D_A, (i.e. the viscous timescale).

6. Discussion

In this paper we have examined the allowable transitions among the 0-, 1-, and 2-vortex spherical Couette flows. The principle methods for studying the transitions are (i) the calculation of the bifurcation diagrams of the steady-state equilibria, (ii) the computation of the most unstable or least stable linear eigenmodes of the steady-state flows, and (iii) the numerical calculation of the velocity during the transitions with the initial-value code. We believe that this paper is the first to calculate the $0 \to 1$ and the $2 \to 1$ transitions and also the first to present the details of the velocity field during the $1 \to 0$ and $0 \to 2$ transitions.

Our initial-value experiments provide us with a set of empirical rules that govern transitions among spherical Couette flows. These rules appear also be be obeyed in transitions among Taylor–Couette flows in finite cylinders (Mullin 1982). The rules are:

(i) A single Taylor vortex can form at a stagnation point in a vortex with a pinch. When it appears initially it has zero circumferential (or, for cylindrical flows, axial) length and has a circulation opposite to that of the flow in the original vortex. The newly created Taylor vortex divides the flow in the original vortex into two pieces,

each piece becoming a vortex with circulation in the same direction as the original vortex. In this process one vortex with a stagnation point becomes transformed into three abutting vortices with circulations that alternate in sign.

(ii) The reverse of rule (i): A single Taylor vortex between two other vortices can decrease its circumferential (or axial) length to zero and disappear, being replaced by a pinch or stagnation point.

(iii) A pair of abutting Taylor vortices separated by a radial inflow boundary can shrink their circumferential (or axial) length to zero, disappear, leaving a radial outflow boundary between two other vortices.

The $0 \rightarrow 2$ transition is an example of the first rule with the process described in (i) occurring simultaneously in both hemispheres.

The $0 \rightarrow 1$ transition uses rule (i) but only in one hemisphere and is therefore asymmetric. The $2 \rightarrow 1$ transition is also asymmetric and uses rule (ii) in just one hemisphere. The $1 \rightarrow 0$ transition uses rule (iii) at the equator so that the $1 \rightarrow 0$ transition is also symmetric. Ignoring these three rules we could produce scenarios for several never-observed transitions. For example, we could produce a symmetric $0 \rightarrow 1$ transition by creating a pair of Taylor vortices at the outflow radial boundary at the equator.

We know of no theoretical way of deriving our three rules, although the physics described by these rules is not very surprising. For example, rule (i) just describes the formation of recirculation vortices at stagnation points. This is a very common hydrodynamical process when the local *Re* of a stagnation point is of order 10 (cf. Taneda 1979). What is surprising and hard to understand from a theorist's point of view is the large number of ways that vortices could form that are not included in our set of rules. For example, there is no mathematical proof that the axisymmetric flow along an unstable outflow boundary cannot form a pair of axisymmetric Taylor vortices. However, we note that it has been observed numerically that an axisymmetric cylindrical Taylor–Couette flow with a locally unstable outflow boundary produces non-axisymmetric waves rather than a new pair of axisymmetric Taylor vortices (Marcus 1984). Of course, we must also leave open the possibility that more rules will have to be added to our set when new transitions among cylindrical or spherical Couette flows are observed or simulated in the future.

Our bifurcation diagrams along with the linear eigenmode calculations allow us to explain why the laboratory experiments of Wimmer (1976) and K. Bühler (private communication, 1983) can only produce the $0 \rightarrow 2$ (or $2 \rightarrow 0$) transition when the acceleration (or deceleration) of the inner sphere is rapid and always produces the $0 \rightarrow 1$ (or the $2 \rightarrow 1$) transition when the acceleration (or deceleration) is slow. Our explanation, given in §3, is based on the fact that the 0-and 2-vortex flows lie along the same equilibrium curve and the 1-vortex equilibrium is distinct. The $0 \rightarrow 1$ and $2 \rightarrow 1$ transitions are slow, and the Reynolds number regime where the 0- and 2-vortex flows are unstable is very small. With fast accelerations of the inner sphere, it is possible for experimentalists to pass through the unstable part of the 0- and 2-vortex equilibrium curve before the instability leading to the 1-vortex flow has a chance to act. The agreement between our predictions of the critical Reynolds numbers for transition and the laboratory experiments is extremely good.

Our linear calculations, including the stability analysis of the Stokes flow, provide us with strong evidence that the instabilities that cause the $0 \rightarrow 1$ and $2 \rightarrow 1$ transitions are due to the same physical mechanisms, and that it is the centrifugal instability of the azimuthal component of the velocity and not the meridional flow

associated with the stagnation points and recirculation vortices that initially cause the instability.

One example of a finding of our study that uses all of our numerical tools is our prediction of the timescales associated with transition. The $0 \rightarrow 1$ transition proceeds slowly at first because the linearly unstable eigenmode must grow from its small initial amplitude (due to the antisymmetric noise present in both the laboratory and the numerical experiments) to an amplitude sufficiently large so that the characteristic *Re* of the eigenmode is greater than unity and nonlinear phenomena can occur. The time associated with this part of the transition is easily calculated with our eigenvalue solver. The nonlinear part of the transition where the stagnation point forms the recirculation vortex is best examined with our initial-value solver. Our analysis in §5 of how energy is transferred out of the antisymmetric composition of the velocity explains the long timescale for the re-establishment of the reflection-symmetry at the end of the transition.

The breaking of symmetry (about the equatorial plane) is of some importance in this study, so it would be useful to have a direct comparison of the numerically predicted symmetry breaking and a laboratory measurement. Torque measurements (which are functions only of the reflection-symmetric component of the velocity) cannot be used. Perhaps the easiest laboratory observation would be to measure the correlation of the velocity between two points on opposite sides of the equator. The positions of the two velocity probes can be adjusted by requiring that the two velocities be equal for steady-state (reflection-symmetric) flows. The anti-symmetric component of the velocity during transition can then be measured directly and compared with numerical calculations.

We thank K. Bühler, S. Orszag, G. Schrauf, and M. Wimmer for useful discussions. This work was supported in part by National Science Foundation Grants MEA-82-15695, MEA-84-10412, AST-82-10933, and AST-84-12170. The numerical calculations were done on the CRAY-1 computers at the National Center for Atmosphere Research (NCAR) which is operated by the National Science Foundation.

REFERENCES

ASTAF'EVA, N. M., VVEDENSKAYA, N. D. & YAVORSKAYA, I. M. 1978 Numerical study of nonlinear axisymmetric flow of fluid between two concentric rotating spheres. In *Sixth Intl Conf. on Num. Methods in Fluid Dyn.* (ed. H. Cabannes, M. Holt, & V. Rusanov), Lecture Notes in Physics, vol. 90. Springer.

BARTELS, F. 1982 Taylor vortices between two concentric rotating spheres. *J. Fluid Mech.* **119**, 1–25.

BENJAMIN, T. B. 1976 Applications of Leray–Schrauder degree theory to problems of hydrodynamic stability. *Math. Proc. Camb. Phil. Soc.* **79**, 373–392.

BENJAMIN, T. B. 1978*a* Bifurcation phenomena in steady flows of a viscous fluid. I: Theory. *Proc. R. Soc. Lond.* A **359**, 1–26.

BENJAMIN, T. B. 1978*b* Bifurcation phenomena in steady flows of a viscous fluid. II: Experiments. *Proc. R. Soc. Lond.* A **359**, 27–43.

BENJAMIN, T. B. & MULLIN, T. 1982 Notes on the multiplicity of flows in the Taylor experiment. *J. Fluid Mech.* **121**, 219–230.

BLENNERHASSETT, P. J. & HALL, P. 1979 Centrifugal instabilities of circumferential flows in finite cylinders: linear theory. *Proc. R. Soc. Lond.* A **365**, 191–207.

BONNET, J. P. & ALZIARY DE ROQUEFORT, T. 1976 Ecoulement entre deux sphères concentriques en rotation. *J. Méc.* **15**, 373–397.

BRATUKHIN, I. K. 1961 On the evaluation of the critical Reynolds number for the flow between two rotating surfaces. *J. Appl. Math. Mech.* **25**, 1286–1299. (Transl. *Prikl. Mat. i Mekh.* **25**, 858–866.)

DENNIS, S. C. R. & QUARTAPELLE, L. 1984 Finite difference solution to the flow between two rotating spheres. *Computers and Fluids* **12**, 77–92.

JOSEPH, D. D. 1981 Hydrodynamic stability and bifurcation. In *Hydrodynamic Instabilities and the Transition to Turbulence* (ed. H. L. Swinney & J. P. Gollub), pp. 27–76. Springer.

KHLEBUTIN, G. N. 1968 Stability of fluid motion between a rotating and a stationary concentric sphere. *Fluid Dyn.* **3**, 31–32. (Transl. *Izv. AN SSSR Mekh. Zhidkosti i Gaza* **3**, 53–56.)

KIRCHGÄSSNER, K. & SORGER P. 1968 Stability analysis of branching solutions of the Navier–Stokes equations. In *Proc. Twelfth Intl Congress of Applied Mechanics* (ed. M. Hetényi & W. G. Vincenti). Springer.

KOGELMAN, S. & DI PRIMA, R. C. 1970 Stability of spatially periodic supercritical flows in hydrodynamics. *Phys. Fluids* **13**, 1–11.

MARCUS, P. S. 1984 Simulation of Taylor-Couette flow. Part 2. Numerical results for wavy-vortex flow with one travelling wave. *J. Fluid Mech.* **146**, 65–113.

MARCUS, P. S. & TUCKERMAN, L. S. 1987 Simulation of flow between two concentric rotating spheres. Part 1. Steady states. *J. Fluid Mech.* **185**, 1–30.

MULLIN, T. 1982 Mutations of steady cellular flows in the Taylor experiment. *J. Fluid Mech.* **121**, 207–218.

MUNSON, B. R. & JOSEPH, D. D. 1971 Viscous imcompressible flow between concentric rotating spheres. Part 2. Hydrodynamic stability. *J. Fluid Mech.* **49**, 305–318.

MUNSON, B. R. & MENGUTURK, M. 1975 Viscous incompressible flow between concentric rotating spheres. Part 3. Linear stability and Experiments. *J. Fluid Mech.* **69**, 705–719.

SAWATZKI, O. & ZIEREP, J. 1970 Das Stromfeld im Spalt zwischen zwei konzentrischen Kugelflächen, von denen die innere rotiert. *Acta Mechanica* **9**, 13–35.

SCHRAUF, G. 1983*a* Branching of Navier–Stokes equations in a spherical gap . In *Proc. 8th Intl Conf. Numerical Methods in Fluid Dyn. Aachen 1983*, pp. 474–480. Springer.

SCHRAUF, G. 1983*b* Lösungen der Navier–Stokes Gleichungen für stationäre Strömungen im Kugelspalt. Ph.D. thesis, Universität Bonn.

SCHRAUF, G. & KRAUSE, E. 1984 Symmetric and asymmetric Taylor vortices in a spherical gap. In *Proc. 2nd IUTAM Symp. on Laminar-Turbulent Transition*. Springer.

SERRIN, J. 1959 On the stability of viscous fluid motions. *Arch. Rat. Mech. Anal.* **3**, 1–13.

SOWARD, A. M. & JONES, C. A. 1983 The linear stability of the flow in the narrow gap between two concentric rotating spheres. *Q. J. Mech. Appl. Maths* **36**, 19–42.

TANEDA, S. 1979 Visualization of separating Stokes flows. *J. Phys. Soc. Japan* **46**, 1935–1942.

TUCKERMAN, L. S. 1983 Formation of Taylor vortices in spherical Couette flow. Ph.D. thesis, Massachusetts Institute of Technology.

WALTON, I. C. 1978 The linear stability of the flow in a narrow spherical annulus. *J. Fluid Mech.* **86**, 673–693.

WIMMER, M. 1976 Experiments on a viscous fluid flow between concentric rotating spheres. *J. Fluid Mech.* **78**, 317–335.

YAKUSHIN, V. I. 1969 The instability of fluid motion of a liquid in a thin spherical layer. *Fluid Dyn.* **4**, 83–85. (Transl. *Izv. AN SSSR, Mekh. Zhidkosti i Gaza* **4**, 119–123.)

YAVOSKAYA, I. M., BELYAEV, Y. N., MONAKHOV, A. A. 1977 Stability investigation and secondary flows in rotating spherical layers at arbitrary Rossby numbers. *Sov. Phys. Dokl.* **22**, 717–719. (Transl. *Dokl. Akad. Nauk SSSR* **237**, 804–807.)